Università degli Studi di Padova

DEPARTMENT OF INDUSTRIAL ENGINEERING
Master degree course in Electrical Engineering

THERMOGRAPHIC DETECTION OF SURFACE CRACKS BY INDUCTION HEATING

SUPERVISOR:
Dr. Eng. Michele Forzan

CO-SUPERVISOR:
Dr. Eng. Cristian Pozza

GRADUATE:
Martino Spadetto

AY 2013/2014

Même le soleis a ses taches.
Napoléon Bonaparte

Ringraziamenti

Desidero ringraziare tutti coloro che mi hanno aiutato nella stesura della tesi con suggerimenti, critiche ed osservazioni: a loro va la mia gratitudine, anche se a me spetta la responsabilitá per ogni errore contenuto in questa tesi.

Ringrazio anzitutto il professor Michele Forzan, Relatore, l'Ing. Cristian Pozza, Co-relatore e l'Ing. Stefano Ghidoni, del laboratorio di Ingegneria dell'Informazione, per l'opportunitá datami nel affidarmi questo progetto di tesi, per l'autonomia e la fiducia che mai ho sentito mancare.

Un ringraziamento particolare ai ragazzi del laboratorio di elettrotermia: Mattia Spezzapria, Alessandro Tolomio, Fernando Bressan e Marco Bullo sempre gentili e disponibili nel aiutarmi anche se oberati dal loro lavoro.

Un grazie ai miei colleghi di studio in particolare Nicoló, Marco, Lorenzo e Federico.

Vorrei infine ringraziare le persone a me piú care: i miei amici, la mia famiglia, i coinquilini della Lough View House di Cork ed infine la mia splendida pavoncina Caterina a cui questo lavoro é dedicato.

Abstract

The aim of this study is the thermographic detection of surface cracks by using induction heating.
The system, through several FEM simulations powered by *Flux*, can be briefly summarized in the following description. An opportune designed inductor, powered by an appropriate alternate current, scans the load's surface. The load, made of conductive material, has been heated by the induced eddy currents, dissipated as heat by Joule effect. In case of defects of the surface of the material, current density, power density and so temperature distribution will be uneven.
This effect is deeply conditioned by the skin depth and the characteristics of the crack. In simple way, surface's defects are visible only if the height of the crack is similar to the penetration depth of the current.
The problem has been solved, analyzing simple models avoiding non linearities and complex geometries. Nevertheless, the tests carried out with different formulations guarantee a good explanation of the general ideas of the method and give useful advices for the continuation of the study.
The test has been divided in seven chapters.

First Chapter

The first chapter describes the different non-destructive testing methods used for quality control.

Second Chapter

The second chapter describes the electromagnetic and thermal theory of the induction heating for a simple cylindrical geometry made of a constant conductive material.

Third Chapter

This chapter describes briefly the Finite Elements Method and the two formulations used in this work.

Fourth Chapter

The fourth chapter shows the results of a first numerical Benchmark analysis of the problem, where a simple brick load made of steel is heated with induction heating. The results given from the simulations are then used for a magneto-thermal analysis of a brick load cracked in the surface.

Fifth Chapter

In this chapter the Surface Impedance formulation is use to simulate an automatic system for crack detection that used a pancake coil.

Sixth Chapter

In this chapter, the previous analysis of an automatic system for crack detection is studied for an hairpin inductor.

Seventh Chapter

In this chapter the conclusions and the work to do are presented.

Sommario

Scopo di questo lavoro é iniziare, attraverso una serie di simulazioni FEM, condotte mediante il programma *Flux*, l'analisi di fattibilitá di un sistema di rilevazione di cricche superficiali attraverso il riscaldamento ad induzione.
Il sistema simulato puó essere brevemente riassunto dalla seguente descrizione.
Un conduttore, opportunamente dimensionato e alimentato, trasla al di sopra della superficie del pezzo da testare. Il provino, di materiale conduttivo, risulta pertanto sede di correnti indotte che dissipandosi in calore, per effetto Joule, innalzano la temperatura del provino.
A seconda che la superficie del pezzo in esame presenti o meno cricche, si rileveranno discontinuitá nella distribuzione sia della densitá di corrente, che della densit di potenza e quindi anche della temperatura.
L'effetto, come si vedrá nelle simulazioni, é visibile solo se la corrente risulta disposta in uno spessore di penetrazione di dimensione confrontabile con la profonditá della cricca.

Le maggiori difficoltá, come é facilmente pensabile, sono state riscontrate durante discretizzazione della geometria. Al fine di risolvere il problema, ci si concentrati sulla risoluzione di un problema fortemente semplificato sia nella geometria che nelle proprietá fisiche del materiale.
Le diverse formulazioni impiegate, hanno peró comunque permesso di definire alcune linee guida fondamentali, utili per la prosecuzione dello studio del fenomeno.
Il lavoro che segue é suddiviso in sette parti principali.

Primo Capitolo

Nel primo capitolo sono presentati i diversi metodi non distruttivi abitualmente impiegati per il controllo di qualit.

Secondo Capitolo

Nel secondo capito si discute la teoria elettromagnetica e termica del riscaldamento ad induzione per un cilindro caratterizzato da conducibilit elettrica

costante.

Terzo Capitolo

Il terzo capitolo descrive il metodo degli elementi finiti e accenna brevemente alla descrizione delle due diverse formulazioni impiegate nello studio del problema.

Quarto Capitolo

In questo capitolo sono riportati i risultati ottenuti per un parallelepipedo riscaldato ad induzione. I risultati sono poi serviti per simulare il riscaldamento ad induzione di un provino a forma di parallelepipedo, questa volta superficialmente criccato.

Quinto Capitolo

Lo studio preliminare del quarto capitolo stato ampliato valutando la possibilitá di rilevare cricche superficiali in modo automatico utilizzando un pancake coil.

Sesto Capitolo

Le stesse simulazioni condotte nel capitolo precedente sono state quindi ripetute cambiando la forma dell'induttore, non piú a pancake ma fatto ad hairpin.

Settimo Capitolo

Nel settimo e ultimo capitolo sono brevemente ripetute le conclusioni delle singole esperienze e suggeriti i lavori futuri che sarebbe interessante sviluppare.

Contents

List of Figures

List of Tables

Part I

Theory

Chapter 1

Non-Destructive Testing

1.1 Introduction

By definition Non-Destructive Testing (NDT) is the *use of noninvasive techniques to determine the integrity of a material, component or structure.*
In contrast to NDT, other tests are destructive. These destructive tests are often used to determine the physical proprieties of the materials such as impact resistance, ductility, fracture toughness and fatigue strength, but discontinuities and differences in material characteristics are more effectively found by NDT.
Non-destructive techniques are ever-increasing used in quality control procedures because they do not impair the usefulness of the material and so they can be applied on a sampling basis for individuals investigation or may be used for 100% checking.
Nowadays nondestructive tests are used in manufacturing, fabrication and in-service inspections to ensure:

- product integrity and reliability;
- quality control of manufacturing processes;
- lower production costs;
- uniform quality level;
- prevention of accidents, as can be seen in figure 1.1;
- improving of the performances;
- improving of the project's specifications.

What follows is a brief description and comparison of the common used methods.

Figure 1.1: Viareggio train derailment: 32 deaths, injuries 26. (29 June 2009)

1.2 Visual Inspection

Visual Inspection (VI) is the oldest and the simplest of all the non-destructive methods. During the inspection, the components are visually scanned, sometimes with the aid of lenses, fibrescopes, cameras and video equipment. In this kind of tests is evident the importance of the knowledge and the experience of the technician.
Visual inspections is used for surface's defects detection only.
The main advantages of VI are:

- cheap analysis;
- the method is suitable for all materials.

The main disadvantage are:

- the subjectivity of the method. Analysis is based on technician's experience and skills;
- the impossibility of testing samples with no directly accessible surface.

1.3 Dye Penetrant Inspection

Dye Penetrant Inspection (DPI), also called Liquid Penetrant Inspection (LPI) or Penetrant Testing (PT), is a non destructive test based upon capillary action. It is used to detect surface's defects such as hairline cracks, surface porosity, leaks in new products, and fatigue cracks on in-service components, that are not visible to the naked eye.
The steps of the process, displayed in figure 1.2, can be listed as follow:

1. **pre-cleaning** of the sample's surface, in order to remove any dirt, paint or oil that could cause false indications;
2. **application of penetrant**;
3. **removal of excess surface penetrant**. The removal method depends on the type of penetrant used: water-washable, solvent-removable, etc;
4. **developer application**, the developer draws penetrant from defects out onto the surface to form a visible indication;
5. **inspection** of the sample's surface through visible light or ultraviolet light of adequate intensity;
6. **post cleaning** of the sample.

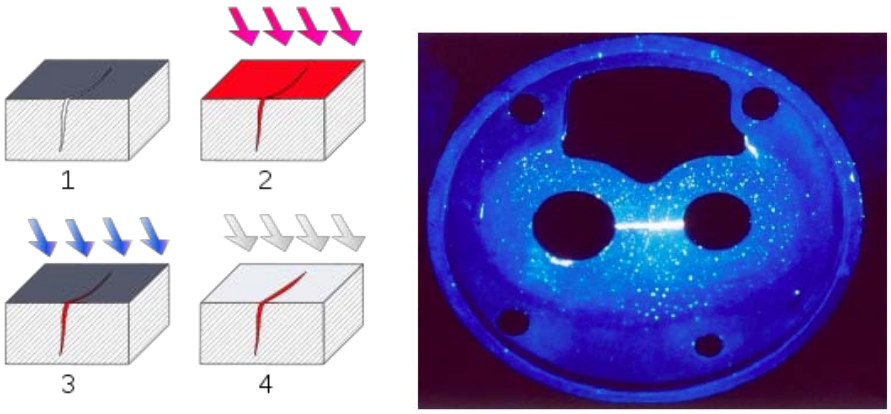

Figure 1.2: In the right: (1) Section of material with a surface-breaking crack. (2) Penetrant is applied to the surface.(3) Excess penetrant is removed. (4) Developer is applied, rendering the crack visible. In the left: Dye Penetrant Inspection test, the crack is visible.

As VI, DPI can be used on virtually any material even if it is used predominantly on nonferrous materials, furthermore this method reveals flaws that are physically open to the surface. Therefore surface preparation is critical to the effectiveness of this inspection method. DPI is slower to perform than the ultrasonic method, but the results are very clearly visible to the technician.

1.4 Magnetic Particle Inspection

Magnetic Particle Inspection (MPI) is used to detect surface and slightly subsurface discontinuities only in ferromagnetic materials.

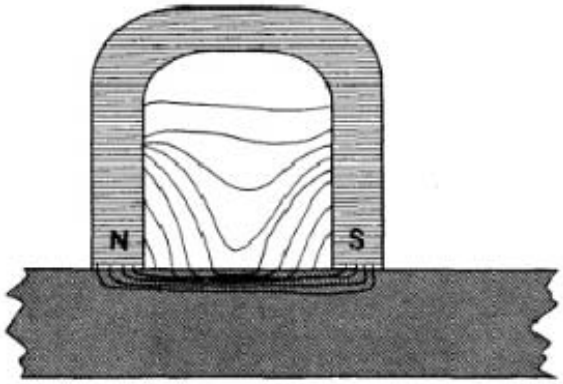

Figure 1.3: Magnetic Particle Inspection test

The general steps of the test can be resumed as follow:

1. **cleaning** of the part, in order to remove oil and other contaminants;
2. **magnetization** of the part;
3. **inspection** of the part with UV light;
4. **demagnetization** of the part;
5. **new test** with another orientation of the magnetic field, if required.

1.5 Radiography Testing

Radiography Testing (RT), is used to view the internal structure of a non-uniformly composed and opaque object. RT uses the ability of short *X-rays* and γ*-rays* to penetrate various materials. RT can be used for all the materials, but defects such as cracks perpendicular to the radiation beam cannot be detected. Lack of accessibility due to object/weld configuration may, however, preclude the use of this method.
The main advantages of RT can be summarized in the following list:

- possibility of volumetric discontinuities detections;
- informations are presented pictorially;
- a permanent record is provided, which could be viewed at a time and place distant from the test;
- the method can be used on any material.

While the main limitations of RT are:

Figure 1.4: Ultrasonic Flaw Detection test

- the increase in the risk of developing cancer and genetic defects for the human body (protections for operators) after long exposition to RT;
- the beam need to be directed accurately for two-dimensional defects detection;
- the method is not suitable for surface's defects individuation;
- RT needs access to both side of the test object to produce a radiograph;
- the location of defects in test object's cross section is difficult to determine.

1.6 Ultrasonic Flaw Detection

Ultrasonic Flaw Detection (UFD), or Ultrasonic Testing (UT), uses very short ultrasonic pulse-waves, transmitted into materials to detect internal flaws or to characterize materials.
Ultrasonic testing, figure 1.4, is usually used on steel or other metals, but it can be also used on concrete, wood and composites.
UT uses the propagation and reflection of the ultrasonic waves to detect both surface and sub-surface defects. These reflections are transformed back into an electrical signal by a transducer, and the results are displayed on screen.

The advantages of ultrasonic test are:

- high sensitivity of the method, that permits the detection of minute defects;
- a great penetrating power optimal for surface and sub-surface analysis;
- the method guarantee fast response.

Even if UT is one of the most used non destructive techniques, some test conditions may limit the application of the method. Usually UT limitations relate to:

- unfavourable geometry;
- undesirable material structure.

1.7 Eddy Current Testing

Eddy Current Testing (ET) is commonly used for the detection of surface or subsurface flaws and conductivity measurement.
ET can only be applied on conductive materials and it is extremely sensitive to the material characteristics: conductivity, permeability and dimensions. The method can be summarize in its main steps as follow:

- a coil is powered by an alternate current;
- the alternate current creates an alternate magnetic field;
- this alternate magnetic field induce eddy currents in the load;
- the presence of defects modifies the magnitude and the phase of the eddy currents;
- the defect is detected as a change in the impedance.

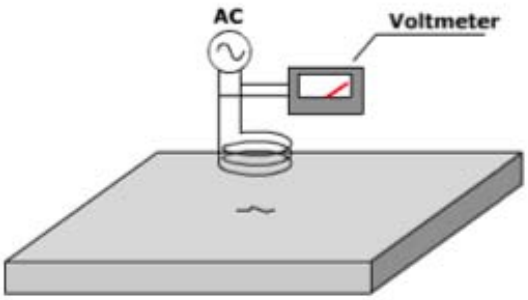

Figure 1.5: Eddy Current Method

1.7.1 Thermographic Eddy Current Method

The circulation of eddy currents inside the material increases the temperature, dissipating heat by Joule losses. The temperature distribution, almost like the impedance, depends on the characteristics of the samples. This means that any defects in the surface or subsurface can be detected as change of impedance and also as change in temperature distribution.
Good thermal imaging cameras measure a temperature difference of $0.1°C$. This method is clearly based on the induction heating and, as induction heating itself, it can be used only on conductive materials.

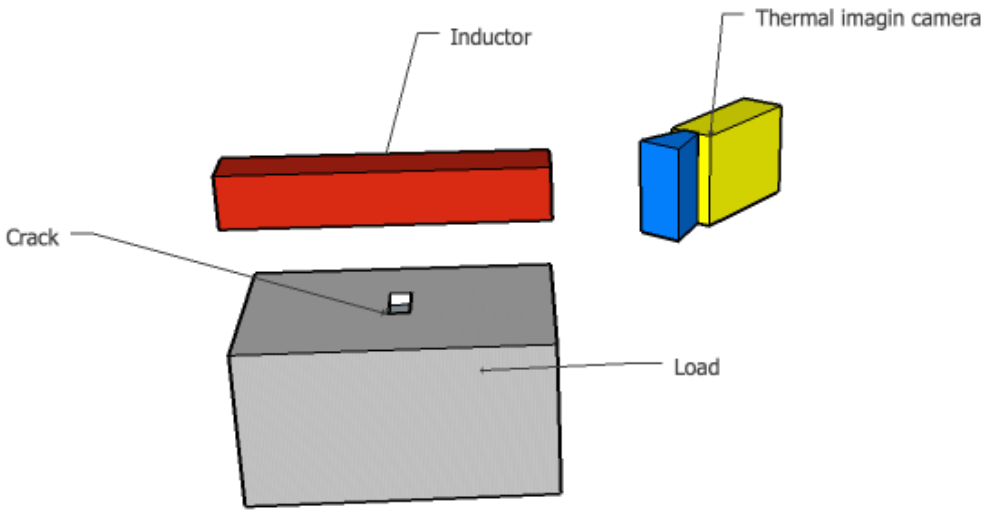

Figure 1.6: Thermal Eddy Current Method

Chapter 2

Induction Heating

2.1 Introduction

Induction heating [2], is the name given to the process of heating a conductive materials, usually metals, by using electromagnetic induction to establish a current in the material. Those induced currents are dissipated as heat for *Joule effect*. It is the energy, stored in the induced currents, responsible of the temperature increasing in the load.
These electric currents induced in the piece by a changing magnetic field in the conductor, are called *eddy currents* or *Foucault currents*.
The distribution of the eddy currents and the heat source, depends on several parameters and conditions and it is always uneven.

Induction heating has been increasingly used, and it is almost irreplaceable in many processes in manufactory industries such as:

- core and contour hardening;
- lamination of hot metals;
- welding;
- metals melting;
- annealing.

In the recent past years, thanks to its versatility, induction heating has been introduced in several fields for unconventional applications, for instance it became an interesting alternative to traditional gas fireplaces with induction cooking systems.
The success of induction heating is easily understandable considering the various advantages of this technology:

- localization of heating in specific zones of the piece, according to the product requirements

- high energy efficiency of process;
- constancy of the finished product characteristics, due to the high repeatability of the process
- fast start, thanks to the lack of thermally inert components;
- short time;
- good environment and working conditions for operators;
- use of a clean and reliable energy source;
- complete automatization of the process.

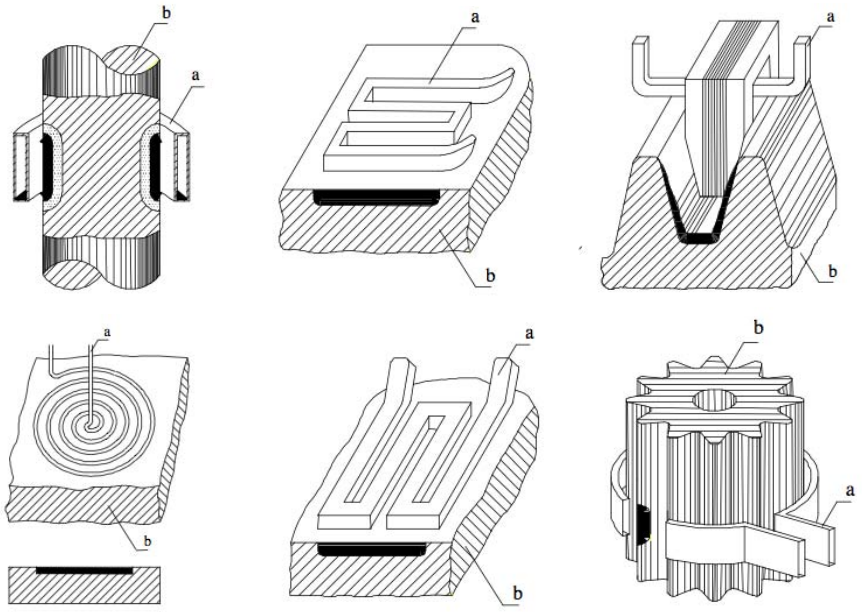

Figure 2.1: Examples of models of inductor *(a)* and load *(b)*

2.2 Electromagnetic Theory

The main principles on which the induction heating process is based, are:

- the induction of eddy currents in the surface's load through electromagnetic induction, according to *Maxwell laws*, by an alternating magnetic field;
- the production of heat directly inside the load due to the dissipation of the eddy currents losses;

- the increase of the temperature inside the load in accordance with *Fourier equations* of thermal conduction.

Nevertheless, it is important to notice that the distribution of the eddy currents and therefore of the temperature, as anticipated in the introduction, is uneven. The depth to which the eddy currents penetrate, and therefore the distribution of heat within the object, depend on the frequency of the primary alternating current and the magnetic permeability, as well as the resistivity of the material.
Under these conditions, it is extremely important to know not only the proprieties of the material, but also to choose adequate values of power, frequency and geometry of the inductor.

A simple case, it is now presented in order to explain the phenomenon in math words.
An induction coil powered by a sinusoidal currents is disposed around a massive cylinder with constant resistivity and permeability. According to

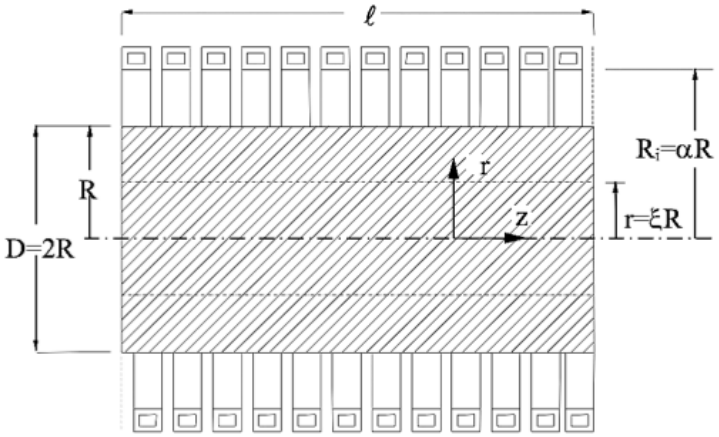

Figure 2.2: Model of inductor and load

the cylindrical coordinates (r, φ, z) the following dimensional parameters are defined:

$$\xi = \frac{r}{R} \quad ; \quad \alpha = \frac{R_i}{R} \tag{2.1}$$

Being the length l a portion of a cylindrical configuration of infinite length, the intensity of the magnetic field in the space between the inductor and the cylinder, characterized by the unique non zero component along z axis, can be expressed as:

$$\dot{H}_0 = \frac{N\dot{I}}{l} \tag{2.2}$$

Ignoring the displacement currents and having for hypothesis sinusoidal values, the Maxwell equations can be written as:

$$\begin{cases} \nabla \times \overline{H} = -\frac{\overline{E}}{\rho} \\ \nabla \times \overline{E} = -j\omega\mu\mu_0\overline{H} \end{cases} \tag{2.3}$$

Conforming with the geometry, the only non zero components are $\dot{H}_z$ and $\dot{E}_\varphi$. Maxwel's equation can be synthesized in:

$$\frac{d^2\dot{H}_z}{dr^2} + \frac{1}{r}\frac{d\dot{H}_z}{dr} - j\frac{\omega\mu_0\mu}{\rho}\dot{H}_z = 0 \tag{2.4}$$

Furthermore, introducing the *skin depth* δ and the adimensional parameter m:

$$\delta = \sqrt{\frac{2\rho}{\omega\mu_0\mu}} \quad ; \quad m = \frac{\sqrt{2}R}{\delta} \tag{2.5}$$

the equation becomes:

$$\frac{d^2\dot{H}_z}{d\xi^2} + \frac{1}{\xi}\frac{d\dot{H}_z}{d\xi} - jm^2\dot{H}_z = 0 \tag{2.6}$$

The solution of this problem, obtained by Bessel equation, is:

$$\dot{H}_z = \dot{H}_0\frac{ber(m\xi) + jber(m\xi)}{ber(m) + jbei(m)} \tag{2.7}$$

As shown in the following graph, fields lines are concentrated mostly in the surface of the cylinder. This behavior is due to the skin effect, and it is more evident for higher value of m.
According to Bessel equation, the current density $\dot{G}$ can be calculated as:

$$\dot{G} = \frac{\dot{E}_\varphi}{\rho} = -\frac{\dot{H}_0}{R}m\frac{ber'(m\xi) + jber'(m\xi)}{ber(m) + jbei(m)} \tag{2.8}$$

Current density is always zero in correspondence of the axis of the cylinder and, the higher is the m, thinner is the surface layer where the current density is concentrated.
The distribution of the specific power induced per unit volume, easily got from the equation of current density, can be written as:

$$w = \rho\dot{G}^2 = w_0\frac{ber'^2(m\xi) + jber'^2(m\xi)}{ber^2(m) + jbei^2(m)} \tag{2.9}$$

As the current density, but with a quadratic decreasing trend, power density is unevenly distributed inside the cylinder and this phenomenon is more evident for higher value of the parameter m.

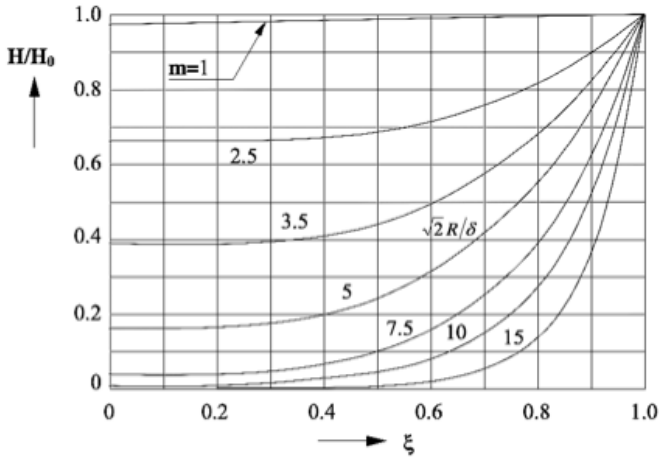

Figure 2.3: Distribution along r of the magnetic field for different values of m

The complex power S, defined by the equation: $S = P + jQ$, can be written according to Bessel equation as the fraction:

$$P + jQ = \frac{ber'm - jber'm}{berm + jbeim} \tag{2.10}$$

Active P_c and reactive Q_c power transmitted trough the electromagnetic field to the cylinder, can be evaluated considering respectively the real and the imaginary part of the *Poynting vector* complex flux.

$$P_c + jQ_c = -\dot{E}_0 \dot{H}_0 2\pi Rl = \dot{H}_0^2 \frac{\rho}{\delta}\sqrt{2}\,(P + jQ)2\pi Rl \tag{2.11}$$

Introducing the reactance x_{i0} of the induction coil in absence of a load for a portion of the length l of a infinitely long configuration:

$$x_{0i} = \omega N^2 \frac{\mu_0^2 \alpha^2}{l} \tag{2.12}$$

It is possible to write $P_c + jQ_c$ as:

$$P_c + jQ_c = \frac{x_{i0}}{2}\mu\,(A + jB)\,I^2 \tag{2.13}$$

Under the hypothesis of an ideal inductor with zero resistance, consisting of a layer of current located to the radius R_i, the reactive power Q_a put in count in the space of air between the load and the inductor is:

$$Q_a = \frac{x_{i0}}{\alpha^2}(\alpha^2 - 1)I^2 \tag{2.14}$$

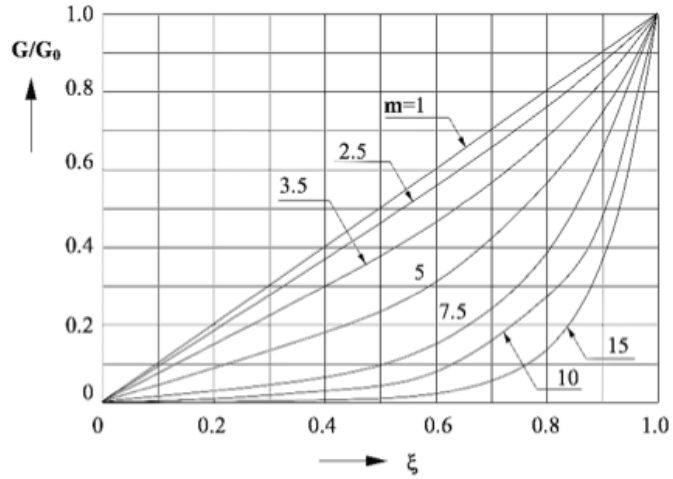

Figure 2.4: Distribution along r of the current density for different values of m

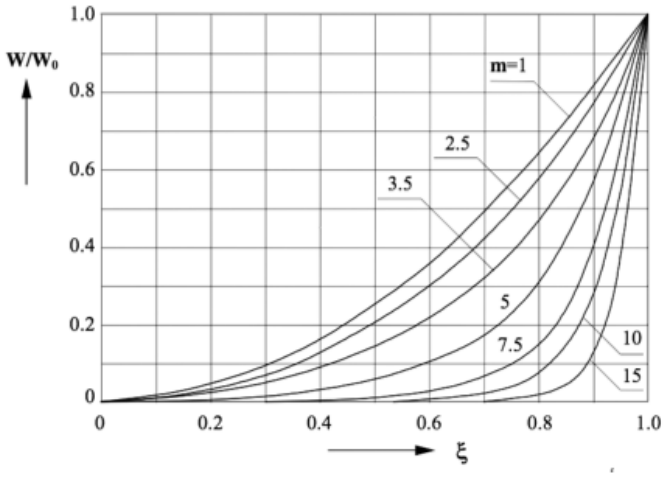

Figure 2.5: Distribution along r of the power density for different values of m

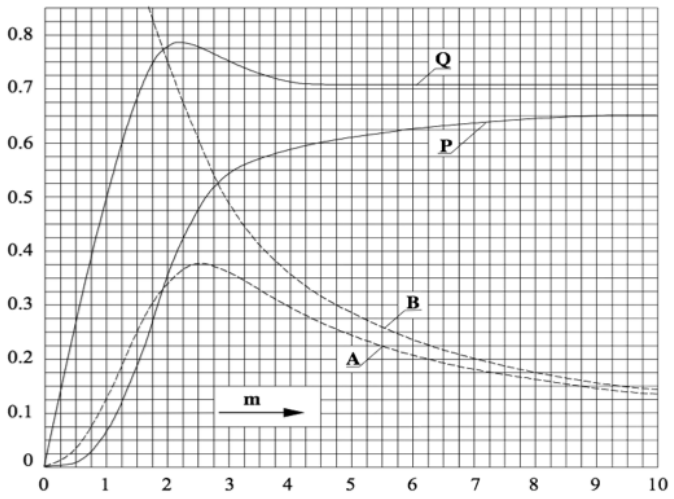

Figure 2.6: Plot of coefficients P,Q and A,B

So the complex power becomes:

$$P_c + j(Q_a + Q - c) = \frac{x_{i0}}{\alpha^2}\{\mu A + j\left[\alpha^2 - (1 - \mu B)\right]\}I^2 \tag{2.15}$$

while the equivalent impedance Z_{e0} is:

$$Z_{e0} = r'_c + j(x_a + x'_c) \tag{2.16}$$

where:

$$r'_c = \frac{x_{i0}}{\alpha^2}\mu A; \quad x'_c = \frac{x_{i0}}{\alpha^2}\mu B; \quad x_a = \frac{x_{i0}}{\alpha^2}(\alpha^2 - 1) \tag{2.17}$$

Using a similar approach, the total power in the inductor can be evaluated with the formula:

$$P_i + jQ_i = H_0^2 \frac{\rho_i}{\delta_i}(A_i + jB_i)2\pi R_i l_i \tag{2.18}$$

where the resistance and the reactance of the inductor are equal to:

$$r_i = x_{i0}\frac{\delta_i}{R_i}A_i k_i; \quad x'_i = x_{i0}\frac{\delta_i}{R_i}B_i \tag{2.19}$$

and k_i is a coefficient greater than one, that considers the axial spaces between the coils.
It is now possible to give an expression to the electrical efficiency of the system load and coil. The electrical efficiency is the ratio between the power directly used to increase the load's temperature and the total active power absorbed by the inductor:

$$\eta_e = \frac{r'_c}{r_i + r'_c} = \frac{1}{1 + \alpha\frac{l}{l_i}\sqrt{\frac{\rho_i}{\rho\mu}}\frac{A_i k_i}{\sqrt{2}P}} \tag{2.20}$$

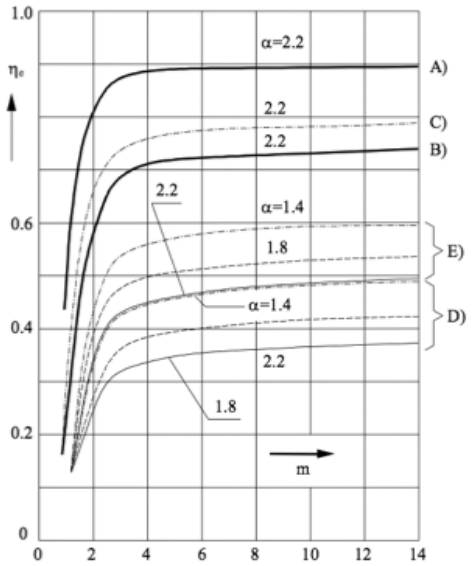

Figure 2.7: Electrical efficiency of the inductor-load system as function of m

The maximum efficiency is obtained for high values of m and $l = l_i$, and it is equal to:

$$\eta_{e,max} = \frac{1}{1 + \alpha\sqrt{\frac{\rho_i}{\rho\mu}}} \tag{2.21}$$

As it is shown in the graph, the electrical efficiency of the inductor, for $m > 2.5$ is virtually frequency independent, while it is clear that for $m < 2.5$ the heating process is not convenient. Moreover, the efficiency changes with α, especially in case of non-magnetic materials or magnetic materials above the Curie point.
Good values of energy efficiency, around 90% are obtained with magnetic steels or high resistivity materials, while the energy efficiency is never above 60% for low resistivity materials.
Another important parameter is the *merit factor*. The merit factor is defined as the ratio between the active power and the reactive power absorbed by the inductor:

$$Q_0 = \frac{x'_c + x_a}{r_i + r'_c} = \frac{\alpha^2 - (1 - \mu B)}{\mu A}\eta_e = Q'_0\eta_e \tag{2.22}$$

where Q_0 is the merit factor for an ideal coil with zero resistance.

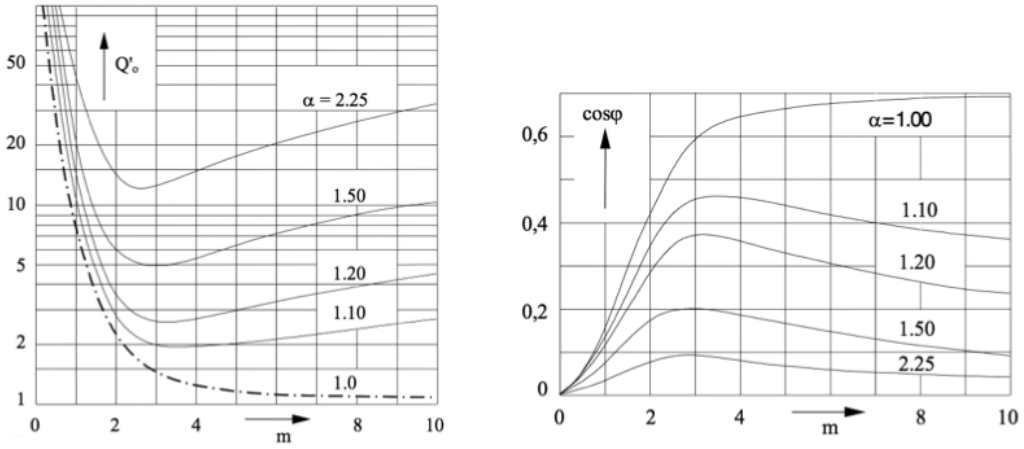

Figure 2.8: Merit factor for zero resistance and power factor as function of m

The power factor is instead evaluated with the formula:

$$cos\varphi = \frac{r_i + r'_c}{\sqrt{(r_i + r'_c)^2 + (x_a + x'_c)^2}} = \frac{1}{\sqrt{1 + (Q'_0 \eta_e)^2}} \tag{2.23}$$

2.3 Skin effect

The distribution of eddy currents and also of the power density is uneven in the load. The depth of heating depends in fact on several parameters, that are:

- the frequency of the ac field;
- the electrical resistivity;
- the relative permeability.

In the following graph the reference depths are shown for different values of temperature. This is because the characteristics of the material depend on the temperature.
This behavior is evident for magnetic materials at the Curie temperature. Above Curie temperature, the magnetic permeability decreases to the value of one, as the material becomes non-magnetic.

2.4 Thermal Theory

Under the hypothesis of a long cylinder, where the transmission of heat is direct only along radial direction and all the thermal parameters of the

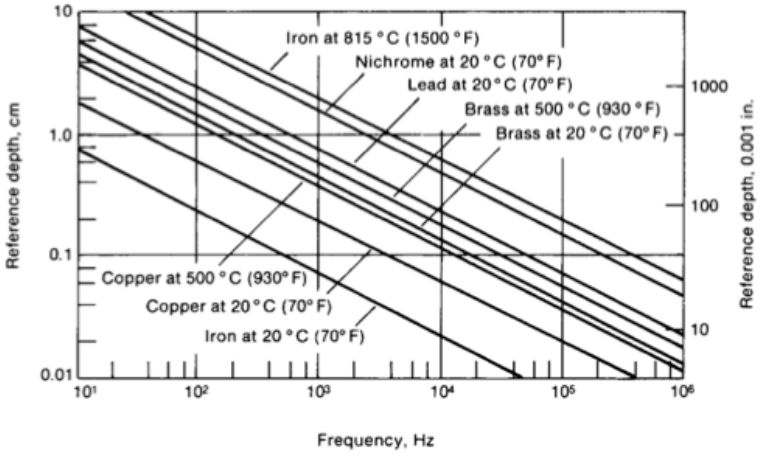

Figure 2.9: Reference depth for various materials

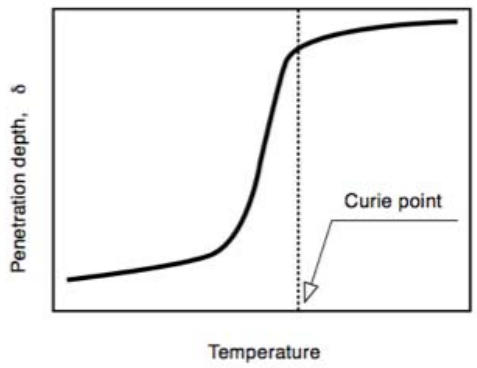

Figure 2.10: Variation of skin depth around Curie temperature

materials are constant, the *Fourier equation* in cylindrical coordinates is:

$$\frac{\partial \vartheta}{\partial t} = k\left(\frac{\partial^2 \vartheta}{\partial r^2} + \frac{1}{r}\frac{\partial \vartheta}{\partial r}\right) + \frac{w(r)}{c\gamma} \tag{2.24}$$

where:

- ϑ is the temperature at the generic radius r after the time t after the heating starts;
- $k = \frac{\lambda}{c\gamma}$ is the *thermal diffusivity*;
- λ is the *thermal conductivity*;
- c is the *specific heat*;
- γ is the *specific weight*;
- $w(r)$ is the *specific power* per unit volume transformed in heat in the cylinder.

The following initial and boundary conditions are given:

$$\begin{cases} \vartheta(r) = 0 & \text{if } t = 0 \\ \frac{\partial \vartheta}{\partial r} = 0 & \text{if } t > 1 \quad \text{and} \quad r = R \end{cases} \tag{2.25}$$

Introducing the following adimensional parameters:

$$\xi = \frac{r}{R}; \quad \tau = \frac{kt}{R^2}; \quad \Theta = \frac{2\pi\lambda}{P_u}\vartheta \tag{2.26}$$

where P_u is the power transformed in heat in the cylinder per axial length unit:

$$P_u = 2\pi \int_{r=0}^{r=R} r w(r)\, dr = 2\pi R^2 \int_{\xi=0}^{\xi=1} \xi w(\xi)\, d\xi \tag{2.27}$$

Defining:

$$\Psi(\xi) = \frac{w(\xi)}{\int_0^1 \xi w(\xi)\, d\xi} = m\frac{ber'^2(m\xi) + bei'^2(m\xi)}{ber(m)ber'(m) + bei(m)bei'(m)} \tag{2.28}$$

It is now possible to write Fourier equation, boundary and initial condition as follow:

$$\frac{\partial \Theta}{\partial \tau} = \frac{\partial^2 \Theta}{\partial \xi^2} + \frac{1}{\xi}\frac{\partial \Theta}{\partial \xi} + \Psi(\xi) \tag{2.29}$$

$$\begin{cases} \Theta(\xi) = 0 & \text{if } \tau = 0 \\ \frac{\partial \Theta}{\partial \xi} = 0 & \text{if } \tau > 0 \quad \text{and} \quad \xi = 1 \end{cases} \tag{2.30}$$

For high frequencies, when the *skin depth* is very small compared to the

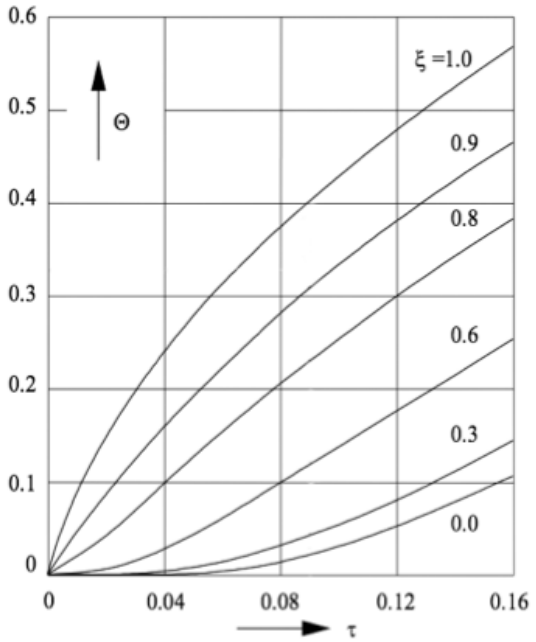

Figure 2.11: Thermal transient for m$\rightarrow \infty$

cylinder's diameter, the surface of the cylinder is the only heated part. In these conditions the equations of the thermal transient become:

$$\Theta = 2\tau + \frac{1}{2}\xi^2 - \frac{1}{4} - 2\sum_{n=1}^{\infty} \frac{J_0(\beta_n \xi)}{\beta_n^2 J_0(\beta_n)} e^{-\beta_n \tau} \tag{2.31}$$

Chapter 3

Finite Elements Method

3.1 Introduction

Finite Elements Method (FEM) is a *numerical method for finding approximate solutions to boundary value problems for differential equations*, [12] [13].
This method is extremely used for solving problems of engineering and mathematical physics. FEM in fact, is exceptionally useful for problems with complicated geometries, loading and material proprieties where analytical solutions can not be obtained.
FEM applies variational methods to minimize an error function, in order to get a stable solution.
FEM is based on a simple assumption: a tough problem can always be divided into an equivalent systems of many smaller problems.
In this case, a model body is discretized by dividing it into an equivalent system of many smaller bodies (finite elements) interconnected at points common to two or more elements and/or boundary surfaces.
The problem is then solved for each element and the total solution is simply reconstructed according to the geometry.
Considering the kind of the problems treated, FEM softwares use different formulations.
Two different formulations used for this work, will be discussed in the next two sections, while the general steps applied during a finite elements analysis will be explained later on.

3.2 AV Formulation

Considering Maxwell equations in the magneto quasi-static case:

$$\begin{cases} \nabla \times \overline{E} = -\frac{\partial \overline{B}}{\delta t} \\ \nabla \times \overline{H} = \overline{J} \\ \nabla \cdot \overline{B} = 0 \\ \nabla \cdot \overline{J} = 0 \end{cases} \tag{3.1}$$

Being the domain Ω simply connected in respect to surface, the *magnetic induction* $\overline{B}$ can be written as:

$$\overline{B} = \nabla \times \overline{A} \tag{3.2}$$

where $\overline{A}$ is called *magnetic vector potential*.
Faraday's law can be written as:

$$\nabla \times \overline{E} = -\frac{\partial(\nabla \times \overline{A})}{\partial t} \tag{3.3}$$

that is equal to:

$$\nabla \times \left(\overline{E} + \frac{\partial \overline{A}}{\partial t} \right) = 0 \tag{3.4}$$

where: $\overline{E} + \frac{\partial \overline{A}}{\partial t}$ is irrotational. If the domain Ω is simply connected with respects to lines, *scalar potential* ∇V can be introduced.

$$\overline{E} = -\nabla V - \frac{\partial \overline{A}}{\partial t} \tag{3.5}$$

The electric field $\overline{E}$ is therefore made of two parts: a conservative one described by the *scalar potential* ∇V, and one due to the variation of the *magnetic vector potential*, $\overline{A}$.
At the same time, according to the constitutive equation: $\overline{J} = \sigma \overline{E}$, the *current density* $\overline{J}$, is made of two parts: $\overline{J} = \overline{J}_s + \overline{J}_{eddy}$, where $\overline{J_s}$ is the source current, that is imposed, while $\overline{J}_{eddy}$ represents the induced current. Being $\overline{H} = \nu \overline{B}$, the constitutive equation that relates the *magnetic field*, $\overline{H}$, to the *magnetic induction*, $\overline{B}$.
With clear meaning of the symbols, $\nabla \times \overline{H}$ and $\nabla \cdot \overline{J}$, equations can be written as follow:

$$\begin{cases} \nabla \times \nu \nabla \times \overline{A} + \sigma \frac{\partial \overline{A}}{\partial t} + \sigma \nabla V = \overline{J}_s \\ \nabla \cdot \left(-\frac{\partial \overline{A}}{\partial t} - \nabla V \right) = 0 \end{cases} \tag{3.6}$$

3.3 Tω Formulation

Considering Maxwell equations in the magneto quasi-static case:

$$\begin{cases} \nabla \times \overline{E} = -\frac{\partial \overline{B}}{\delta t} \\ \nabla \times \overline{H} = \overline{J} \\ \nabla \cdot \overline{B} = 0 \\ \nabla \cdot \overline{J} = 0 \end{cases} \tag{3.7}$$

Being the domain Ω simply connected in respect to surface, the *current density* $\overline{J}$ can be written as:

$$\overline{J} = \nabla \times \overline{T} \tag{3.8}$$

where $\overline{T}$ is called *electric vector potential*.
It is now possible to write $\nabla \times \overline{H} = \overline{J}$ as:

$$\nabla \times \left(\overline{H} - \overline{T}\right) = 0 \tag{3.9}$$

If the domain Ω is simply connected with respects to lines, *scalar potential* $\nabla\omega$ can be introduced.
Therefore the *magnetic field* $\overline{H}$ can be written as:

$$\overline{H} = \overline{T} - \nabla\omega \tag{3.10}$$

Given the constitutive equations: $\overline{E} = \rho\overline{J}$ and $\overline{B} = \mu\overline{H}$, the equations $\nabla \times \overline{E}$ and $\nabla \cdot \overline{B}$ can be written as:

$$\begin{cases} \nabla \times \rho\nabla \times \overline{T} = -\frac{\partial}{\partial t}\left(\mu(\overline{T} - \nabla\omega)\right) \\ \nabla \cdot (\overline{T} - \nabla\omega) = 0 \end{cases} \tag{3.11}$$

3.4 Weighted Residual Method

A general Differential Algebraic Equation (DAE) $\mathcal{L}(U) = 0$, under the hypothesis of domain Ω simply connected with respect to lines and surfaces, can always be written as the following equivalent problem:

$$\mathcal{L}(U) = 0 \longleftrightarrow \int_{\Omega} \omega \left(\mathcal{L}(U)\right) d\Omega = 0 \quad \forall\omega \tag{3.12}$$

This new equivalent problem has the same solution of the original one. In order to find the solution U^*, all the functions U and ω have to be tested. Obviously it is useless to convert a difficult problem into another problem that can not be solved.
The idea is now to find an approximated solution $\widetilde{U}$, nearest to the real U^*,

in the subset of polynomial solutions. In this way the set of the possible solutions contains a limited number of polynomial functions. Each $\widetilde{U}$ is the sum of the evaluated potentials in some nodes, multiplied by a shape function N_i :

$$\widetilde{U} = \sum_i N_i U_i \tag{3.13}$$

Applying the *Galerkin method*, the test functions ω_i are set equal to the shape functions N_i.

$$\omega_i = N_i \quad \text{for} \quad i = 1, ..., n_n \tag{3.14}$$

Being, for instance, the $\mathcal{L}(U)$ a general div-grad equation:

$$\mathcal{L}(U) = \nabla \cdot \epsilon \nabla U \tag{3.15}$$

The problem can be written applying Galerkin Method as:

$$\int_\Omega N_i \nabla \cdot \epsilon \nabla \widetilde{U} \, d\Omega = 0 \tag{3.16}$$

Thanks to the *Green's formula*, the integral becomes:

$$\int_\Omega N_i \nabla \cdot \epsilon \nabla \widetilde{U} \, d\Omega = \int_{\Gamma=\partial\Omega} N_i \epsilon \nabla \widetilde{U} \cdot \overline{n} \, d\Gamma - \int_\Omega \nabla N_i \cdot \epsilon \nabla \widetilde{U} \, d\Omega = 0 \tag{3.17}$$

Under the hypothesis of null boundary term, the previous equation becomes:

$$\int_\Omega N_i \nabla \cdot \epsilon \nabla \widetilde{U} \, d\Omega = - \int_\Omega \nabla N_i \cdot \epsilon \nabla \widetilde{U} \, d\Omega = 0 \tag{3.18}$$

but $\widetilde{U} = \sum_{j=1}^{n_n} N_j U_j$, therefore:

$$\int_\Omega \nabla N_i \cdot \epsilon \nabla \widetilde{U} \, d\Omega = \int_\Omega \nabla N_i \cdot \left(\epsilon \nabla \sum_{j=1}^{n_n} N_j U_j \right) \, d\Omega = 0 \tag{3.19}$$

The summation may be taken out of the integral:

$$\sum_{j=1}^{n_n} \left(\int_{\Omega_e} \nabla N_i \cdot \epsilon \nabla N_j \, d\Omega \right) U_j = 0 \tag{3.20}$$

Being $K_{ij} = \int_{\Omega_e} \nabla N_i \cdot \epsilon \nabla N_j \, d\Omega$, the summation can be written in matrix form:

$$[K] \{U\} = \{0\} \tag{3.21}$$

where $[K]$ is the *Stiffness matrix*.

3.4.1 The Boundary term

The boundary term:

$$\int_{\Gamma=\partial\Omega} N_i \epsilon \frac{\partial \widetilde{U}}{\partial n}\, d\Gamma \tag{3.22}$$

depends on node's position.
What can happen is:

1. the node i is on the boundary:
   (a) Dirichelet condition: do not need to write boundary term.
   (b) Neumann condition:
      i. homogeneous: $\frac{\partial \widetilde{U}}{\partial n} = 0$, boundary term sets to zero.
      ii. non-homogeneous: $\frac{\partial \widetilde{U}}{\partial n} = g$, boundary term is added to the right hand side.
2. the node i is an internal node:
   (a) i is inside a region, ϵ is constant. The boundary term is zero.

$$\int_{\Gamma=\partial\Omega} N_i \epsilon \frac{\partial \widetilde{U}}{\partial n}\, d\Gamma = \int_p^i N_i \epsilon \frac{\partial \widetilde{U}}{\partial n}\, d\Gamma + \int_i^p N_i \epsilon \frac{\partial \widetilde{U}}{\partial n}\, d\Gamma = 0 \tag{3.23}$$

   (b) i is an interface node, ϵ is not constant. The summation of the integrals is set to zero: *weak imposition*.

$$\int_{\Gamma=\partial\Omega} N_i \epsilon \frac{\partial \widetilde{U}}{\partial n}\, d\Gamma = \int_p^i N_i \epsilon_1 \frac{\partial \widetilde{U}}{\partial n}\, d\Gamma + \int_i^p N_i \epsilon_2 \frac{\partial \widetilde{U}}{\partial n}\, d\Gamma = 0 \tag{3.24}$$

Part II

Simulation

Chapter 4

Numerical Benchmark Analysis

The problem has been initially analyzed with an AV Magneto-Thermal analysis of a parametric simple geometry. This preliminary study was really important in order to understand well the problem, discover the limits of the numerical analysis and set good conditions to the variable quantities such as: frequency, distance of the coil and current.

4.1 Geometry

A cracked brick ($Lx \times Ly \times Lz$) made of *Steel*, is heated by a single loop inductor made of copper, located at the distance $D - coil$ from the load's surface and computed from the coil's center. A small surface crack, described as a brick, is located in the middle of the top load's surface. The geometry depicted in the figure 4.1 is described by the following parameters, table 4.1.

Parameter	**Description**	**Formula**	**Value**	**Unit**
Lx	width of the sample	-	10	$[mm]$
Ly	height of the sample	$5Lx$	50	$[mm]$
Lz	depth of the sample	$2Lx$	20	$[mm]$
A	width of the crack	-	3	$[mm]$
B	height of the crack	-	0.06	$[mm]$
C	depth of the crack	-	0.03	$[mm]$
Dcoil	distance between load and coil	-	2	$[mm]$
Lcoil	side of the coil section	-	1	$[mm]$

Table 4.1: Description of geometry of the Benchmark case

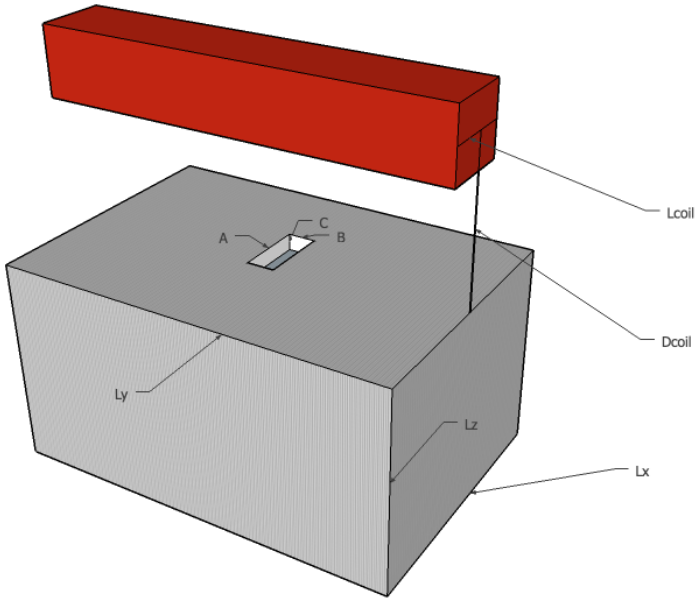

Figure 4.1: Schematic representation of the geometry used in the Benchmark case

4.2 Mesh

The discretization of the geometry is extremely important to get a good solution of the simulation. The mesh has to represent well the physical phenomenon. It has to be fine in the critical points and relaxed where there is no need of a precise discretization. In other words, mesh has to be constituted of small elements in the direction of greater and faster variations of the studied parameter.
In this case, current and temperature distributions are extremely uneven. Therefore mesh has to be fine in the skin depth and near the edges of the defect, while it can be relaxed in the bottom of the load.

4.3 Material Properties

The study has been conducted considering linear materials.
The properties of the inductor, made of copper and always described as *coil conductor*, have been imported from the *Flux library of materials*. The characteristics of the *Steel* viceversa have been chosen *ad hoc*.

4.4 Copper properties

The characteristics of the copper used for all the simulations can be summarize as follow:

1. Electrical property
   (a) Linear temperature dependence
   (b) $\rho_T = \rho_0(1 + \alpha_0(T - T_0))$, where:
      - $T_0 = 0°C$
      - $\rho_0 = \rho_{0°C} = 1.564 \times 10^{-8}$ $[\Omega m]$
      - $\alpha_0 = \alpha_{0°C} = 4.27 \times 10^{-3}$ $[1/°C]$
2. Magnetic property
   (a) Constant permeability
   (b) Relative permeability: $\mu_r = 1$
3. Thermal property
   (a) Thermal conductivity
   (b) $K(T) = 349$ $[W/m°C]$
4. Thermal property
   (a) Constant volumetric heat capacity
   (b) $RCP = 3518000$ $[J/m^3°C]$

4.5 Steel properties

The steel used for all the simulations is a linear steel with the following characteristics.

1. Electrical property
   (a) Isotropic resistivity
   (b) Resistivity: $\rho = 50 \times 10^{-8}$ $[\Omega/m]$
2. Magnetic property
   (a) Linear isotropic permeability
   (b) Relative permeability: $\mu_r = 100$
3. Thermal property
   (a) Thermal conductivity

(b) $K(T) = 35\ [W/m^{\circ}C]$

4. Thermal property
   (a) Constant volumetric heat capacity
   (b) $RCP = 4000000\ [J/m^{3\circ}C]$
5. Mass density
   (a) Constant mass density
   (b) Mass density: $\rho_m = 7800\ [Kg/m^3]$

4.6 Workpiece without crack simulations

Surface defects as cracks, become locations of hot spots when the load is heated by eddy currents. This phenomenon can be visibile or invisible due to many characteristics such as: geometry of the cracks, frequency, the magnitude of the exciting current, etc. For this reason it is important to analyze what happen heating a sample without defects in different conditions. This preliminary analysis is extremely useful in order to choose a set of hypothetical reference parameters for the cracked sample's analysis, that may allow the defect's detection.

4.6.1 Scenario: *D-coil*

The first scenario tested the influence of the coil distance in the temperature distribution. The parameter $D - coil$, that represents the distance from the load's surface to the inductor center, changes from $2[mm]$ to $10[mm]$.

Parameter	Description	Value	Unit
I	current	100	$[A]$
f	frequency	10	$[kHz]$
$D - coil$	distance of the coil	$2 \div 10$	$[mm]$
t	time	1	$[s]$

Table 4.2: Scenario *D-coil* parameters

As expected the electromagnetic coupling between the coil and the load depends on the coil distance.

At the end of the simulation it seems clear that:

- temperature does not increase significantly with $D - coil > 2[mm]$;
- maximum temperature in the surface does not reach $22^{\circ}C$ for $D - coil > 2[mm]$;

- in first approximation, $D - coil$ is fixed to $D - coil = 2[mm]$.

4.6.2 Scenario: *Current*

Chose $D-coil = 2[mm]$, it is now tested the influence of the physical parameter I. The current is deeply connected with the temperature distribution. High currents create high magnetic field and so high eddy currents.
In this scenario, $Current$ changes from 10 up to $100A$, while the other parameters are kept constant.

Parameter	Description	Value	Unit
I	current	$10 \div 100$	$[A]$
f	frequency	10	$[kHz]$
$D - coil$	distance of the coil	2	$[mm]$
t	time	1	$[s]$

Table 4.3: Scenario *current* parameters

Key considerations after the simulation:

- temperature does not increase significantly with $I < 50[A]$. For $I = 50[A]$ the maximum value of temperature in the surface is $21°C$;
- for instance: $I = 100[A]$. This choice may be a limit during the feasibility analysis. The section of the coil used so far in fact may be too small.

4.6.3 Scenario: *Frequency*

Frequency influences the penetration depth of the eddy currents and therefore the temperature distribution. Higher the frequencies, thinner the material's layers where the currents in the surface and the power distribution result concentrated.

Parameter	Description	Value	Unit
I	current	100	$[A]$
f	frequency	$1 \div 100$	$[kHz]$
$D - coil$	distance of the coil	2	$[mm]$
t	time	1	$[s]$

Table 4.4: Scenario *Frequency* parameters

The results of the simulation show that:

- skin depth decreases with high frequencies;
- small cracks may be seen with $f > 10[Khz]$

4.6.4 Hypothetic Reference Scenario Parameters

According to previous simulations, figure 4.2, the following *Reference Scenario Values* have been chosen:

Parameter	Description	Value	Unit
I	current	100	$[A]$
f	frequency	10	$[kHz]$
$D - coil$	distance of the coil	2	$[mm]$
t	time	1	$[s]$

Table 4.5: Hypothetic Reference Scenario parameters

4.7 Workpiece with crack simulations

4.7.1 Reference Scenario

All the previous simulations were repeated for the cracked sample. As expected, cracks are easier to detect using high frequency. Frequency $f = 10kHz$ in particular is not enough to detect the simulated defect.
Time as well is a fundamental parameter. It has to be discretize well. In this case $1[s]$ has been divided in time steps of $\Delta t = 0.1[s]$.
Thermographic detection of surface cracks is conditioned by the thermal condition phenomenon. Long time exposure of induction heating uniforms the temperature distribution. This may impede the detection of hot spots near the edges of the crack.
In order to avoid conduction effects, is necessary to heat the load's surface in a very short time. However the reduction of time obliges high current to keep the same energy's transfer. In conclusion: high current, high frequency and short time.
For this reasons *Hypothetic Reference Scenario parameters* have been modified. The new *Reference Scenario parameters* are resumed in table 4.6.

4.7.2 Scenario: *big-C*

In those simulations, the depth of the crack was increased from $C = 0.03 \div 0.3[mm]$. This scenario reveals a relationship between the skin depth and the depth of the defect. When the skin depth is approximately equal or higher than the depth of the crack, currents near the extremity of the crack

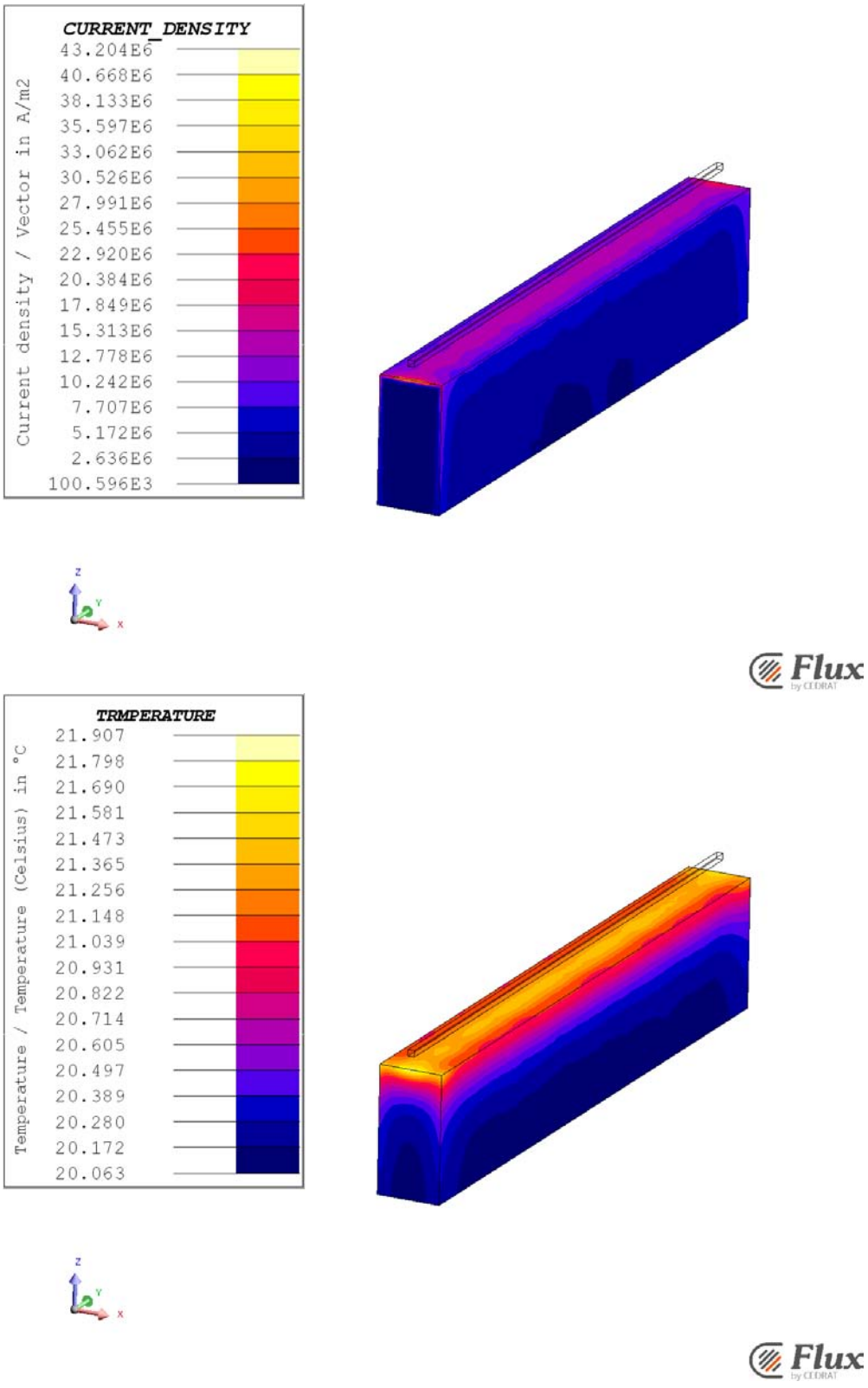

Figure 4.2: Hypothetic Reference Scenario: current density and temperature distribution, $I = 100A$, $D - coil = 2mm$ and $f = 10kHz$

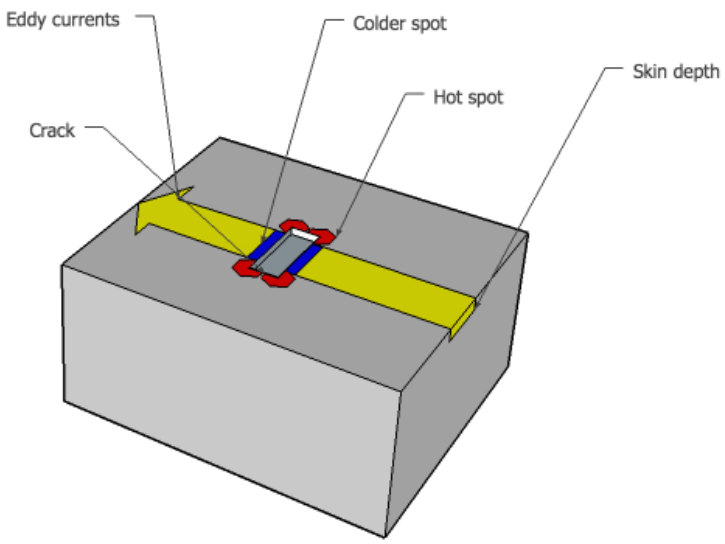

Figure 4.3: High current and power density near the defect

Parameter	Description	Value	Unit
I	current	100	$[A]$
f	frequency	100	$[kHz]$
$D - coil$	distance of the coil	2	$[mm]$
t	time	1	$[s]$

Table 4.6: Reference Scenario parameters

prefers to go alongside the edges of the defects, while when the crack's depth is higher than the skin depth, currents are more likely to pass beneath the defect.

Parameter	Description	Value	Unit
I	current	100	$[A]$
f	frequency	100	$[kHz]$
$D - coil$	distance of the coil	2	$[mm]$
C	depth of the crack	$0.03 \div 0.12$	$[mm]$
t	time	1	$[s]$

Table 4.7: Scenario $big - C$ parameters

This scenario leads to these key considerations:

- at the same frequency, deeper cracks are easier to detect than smaller

ones;

- there is a change in current density [J], that increases its maximum value from $J_{c=0.03} = 32.43 \times 10^6$ to $J_{c=0.12} = 39.88 \times 10^6$;
- even if there is an amplification in the current density, the temperature does not increase much.
- in order to amplify the hot spot effect new simulations will use $f = 400kHz$, the skin depth $\delta = 0.056[mm]$ is now comparable to the crack's depth C.

4.7.3 Scenario: Turn crack

Being $CRICCA-XYZ$ the coordinate system used to build the crack. It is possible to evaluate the problem for different values of α, where α is the tilt angle between the inductor's axis and the crack side A. In this scenario the tilt angle α, changes from 0° to 90°. When $\alpha = 0°$ the crack is perpendicular respect the inductor while, when $\alpha = 90°$, inductor and crack are parallel.

Parameter	**Description**	**Value**	**Unit**
I	current	100	$[A]$
f	frequency	100	$[kHz]$
$D-coil$	distance of the coil	2	$[mm]$
C	depth of the crack	0.03	$[mm]$
t	time	1	$[s]$
α	tilt angle	$0° \div 90°$	–

Table 4.8: Scenario *Turn crack* parameters

Discontinuities are always revealed by the method but of course the defect became less visible when the tilt angle becomes higher, figure 4.5. A reduced portion of the eddy currents in fact faced the defects along its path in the load's surface. The relative position of the crack respects to the inductor is an important aspect to consider during an automatic scansion of the sample's surface.
In both cases, considering the presence of hotspots near the edges of the crack it is possible to measure the width of the defect, evaluating the distance between the two hotspots.

4.8 Considerations on Benchmark case results

Benchmark analysis gave interesting advices and boded well about the possibly of detect surface cracks using induction heating. It is clear that the method works better with high frequency. The obvious choice is to increase

again the frequency, in order to accentuate the uneven distribution of the current density and temperature. Unfortunately the formulation used so far required good volumetric mesh, and the discretization of the skin depth will be extremely laborious and inconvenient. For this reason another formulation is used. This alternative formulation, called *Surface impedance*, does not required a volumetric mesh of the load because the current distribution is evaluated analytically, according to the surface distribution of the current density. Moreover, as shown in the *Turn crack* Scenario, it is important to study the influence of the relative position between defect and inductor.

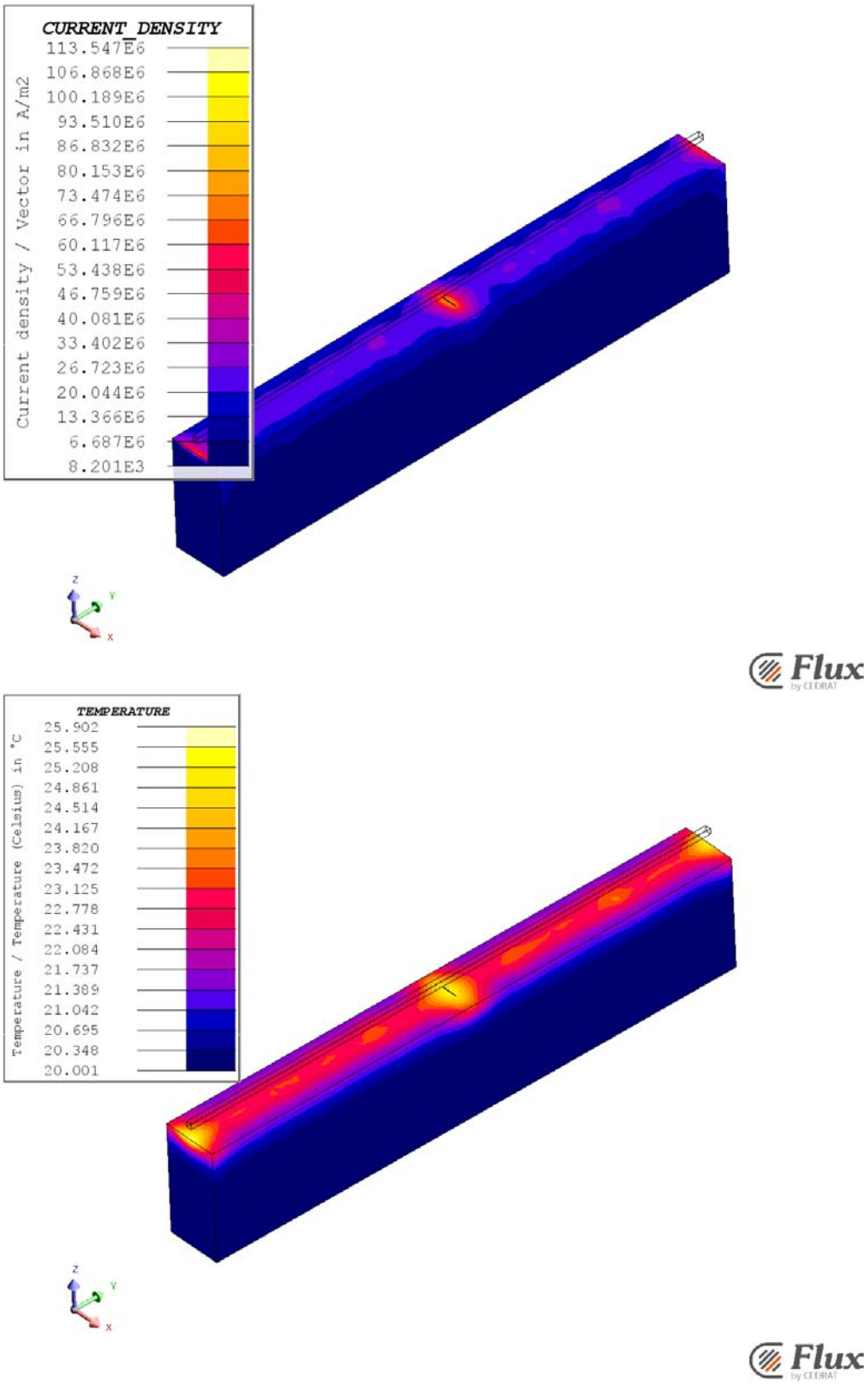

Figure 4.4: Reference Scenario for a cracked load: current density and temperature distribution, $I = 100A$, $D - coil = 2mm$ and $f = 100kHz$

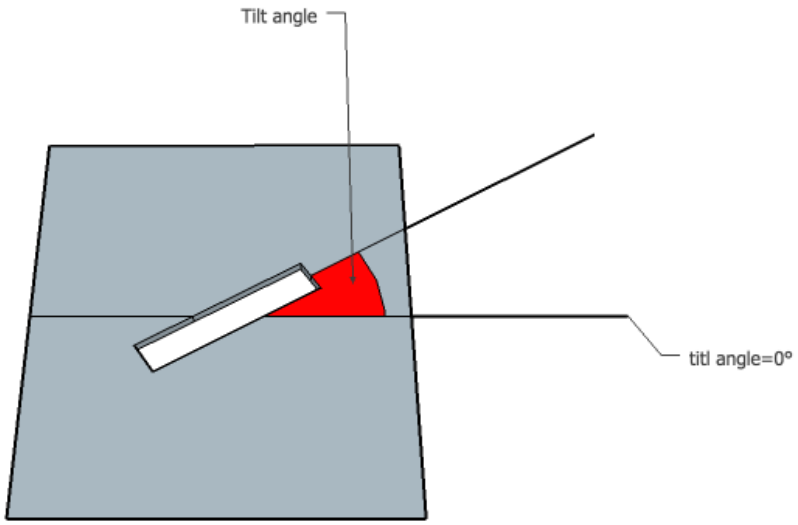

Figure 4.5: Explanation of the Turn Crack Scenario

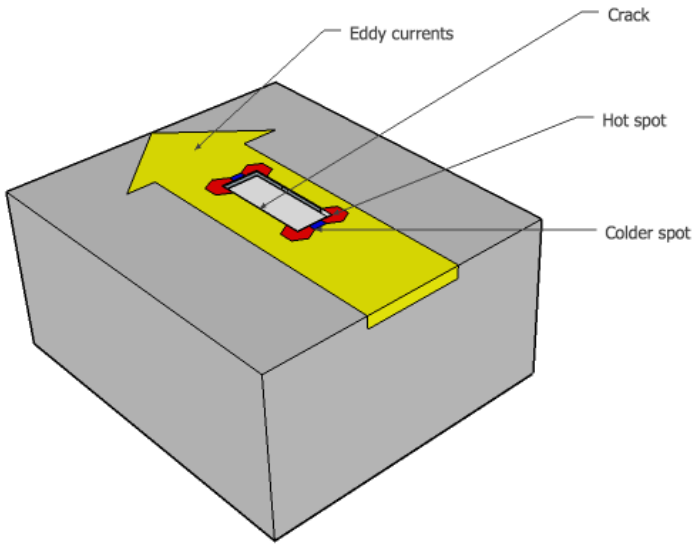

Figure 4.6: Reduction of the hot spot effects for $\alpha = 90°$

Chapter 5

Pancake coil

A wide sheet of *Steel* is scanned with a pancake coil, excited with an high frequency ac current. In order to simulate well the high frequency used, the problem is now studied with the $T\omega$ surface impedance formulation.
The coil translates along both directions x and y. Two different scenarios are evaluated. In the first scenario *Translate-X*, the relative position between the translation sense of the inductor and the crack is amenable to the case $\alpha = 0°$, while in the second scenario *Translate-Y*, $\alpha = 90°$. The crack in both changes the maximum value of current and power density.

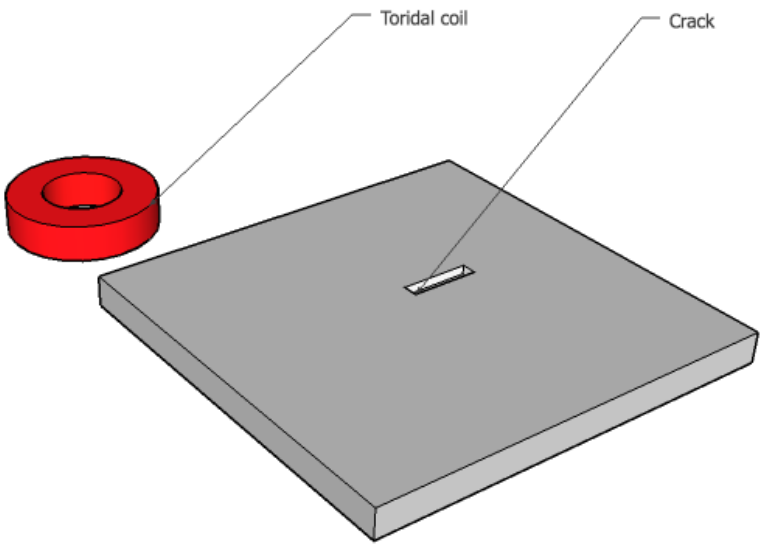

Figure 5.1: Schematic representation of the pancake coil

5.1 Geometry

A cracked wide sheet of *Steel* is heated by a pancake coil. Even in this case, the geometry is described parametrically.

Parameter	Description	Formula	Value	Unit
Lx	width of the sample	-	200	$[mm]$
Ly	height of the sample	$2Lx$	400	$[mm]$
Lz	depth of the sample	$-$	1	$[mm]$
A	width of the crack	-	3	$[mm]$
B	height of the crack	-	0.06	$[mm]$
C	depth of the crack	-	0.03	$[mm]$
Dcoil	distance between load and coil	-	2	$[mm]$
Hcoil	height of the coil	-	15	$[mm]$
Ri	internal hole radius of the coil	-	2.5	$[mm]$
Re	external radius of the coil section	-	10	$[mm]$

Table 5.1: Description of geometry of the pancake coil's case

Coil is built respect the cylindrical coordinate system $COIL-CYL$ defined with respect to the local coordinate system $CRACK-XYZ$, is centered in:

Origin of COIL-CYL	Formula
First component	TRA-X
Second component	TRA-Y
Third component	D-coil

Table 5.2: Origin of coordinate system COIL-CYL

When $Tra-X$ and $Tra-Y$ are both set to zero, the $COIL-CYL$ and $CRACK-XYZ$ lie in the same line $z=0$.

5.2 Mesh

The top load's surface and all the crack faces, without the air's one, are described as surface impedance. There is no need of volumetric mesh of the load. It is however necessary to discretize well the boundaries of the crack. During the scenario mesh has to change with the position of the coil. So it is really important to prevent inconsistent mesh.

5.3 Scenario: Translate X

In this scenario, the coil conductor translates along x direction. In this case, the crack is parallel respects to the coil's translation's direction.

Parameter	Description	Value	Unit
I	current	100	$[A]$
f	frequency	400	$[kHz]$
$D - coil$	distance of the coil	2	$[mm]$
C	depth of the crack	0.03	$[mm]$
$Tra - X$	translation along x	$0 \div 15$	$[mm]$

Table 5.3: Scenario *Translate X* parameters

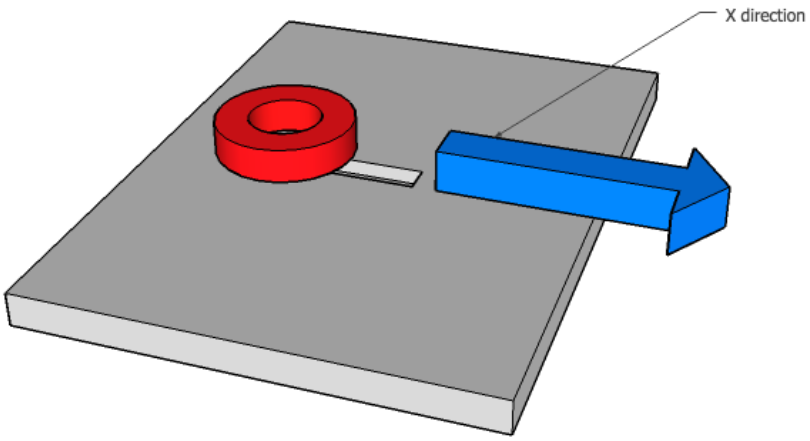

Figure 5.2: Graphic explanation of ScenarioTranslate-X

At the end of the simulation the following considerations can be deduced:

- the current density and the power density evaluated in the point $(A/2; B/2; 0)$ reach the maximum value for $Tra - X \approx 12.5[mm]$, in correspondence of the highest value of eddy currents induced in the load;
- the high frequency of 400 $[kHz]$ amplifies the current and power density near the crack.

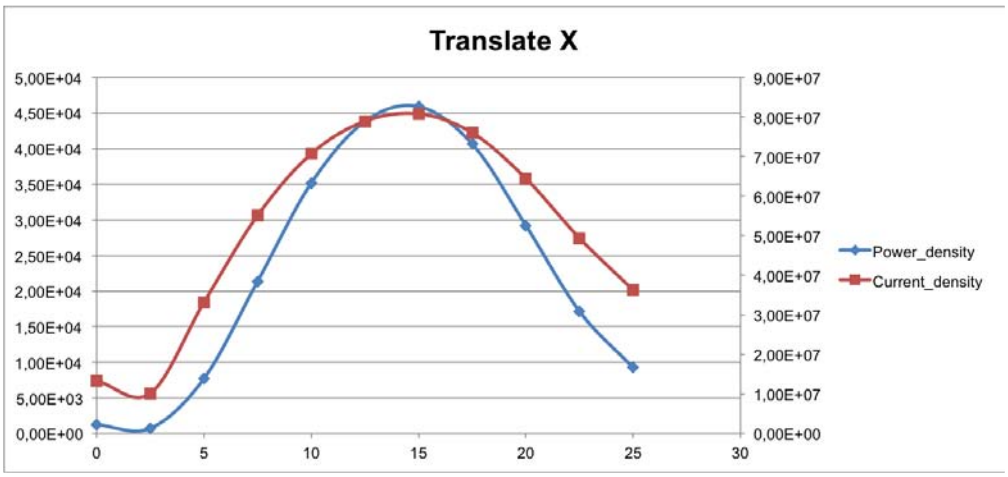

Figure 5.3: Variation of the current and power density in function of Tra-X

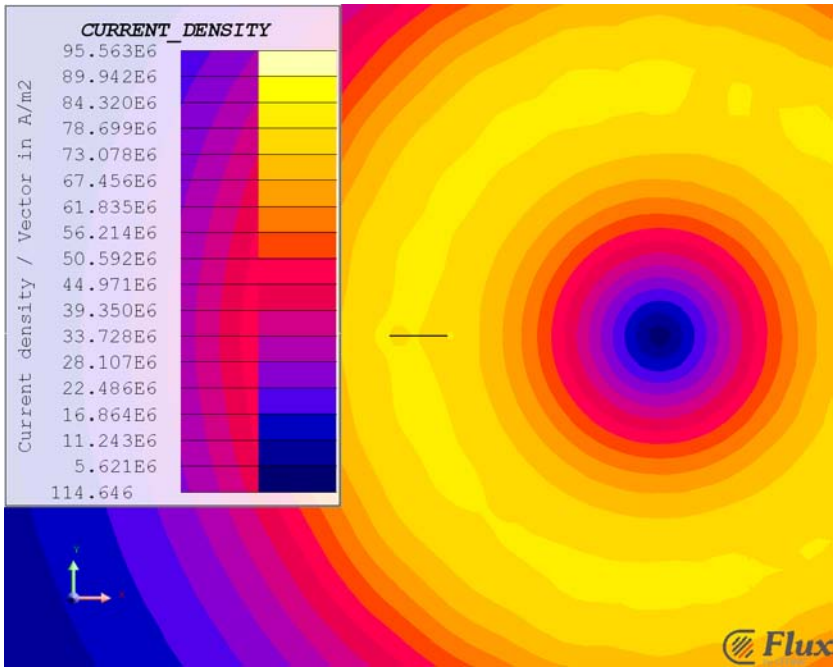

Figure 5.4: Current density distribution for Tra-X=12.5[mm]

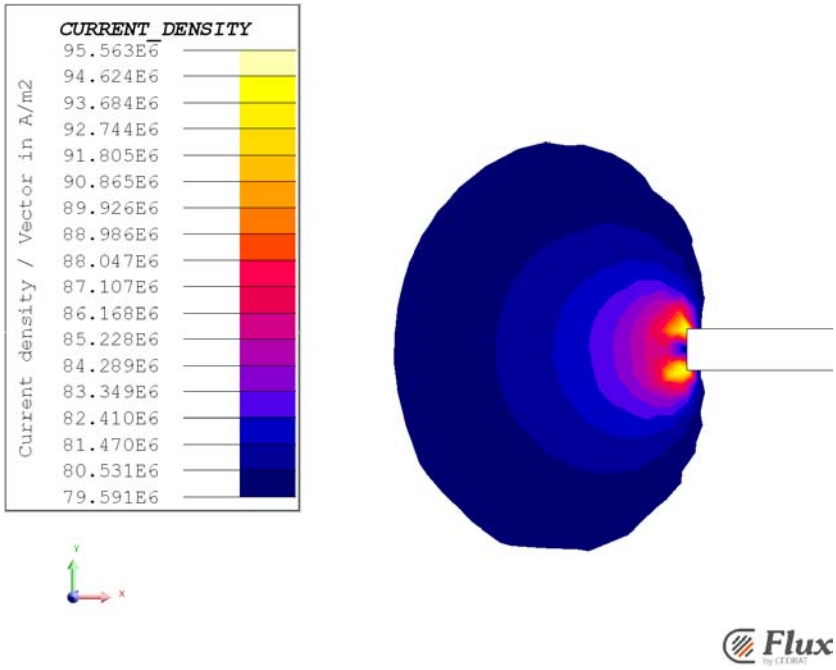

Figure 5.5: Current density distribution near the crack, Tra-X=12.5[mm]

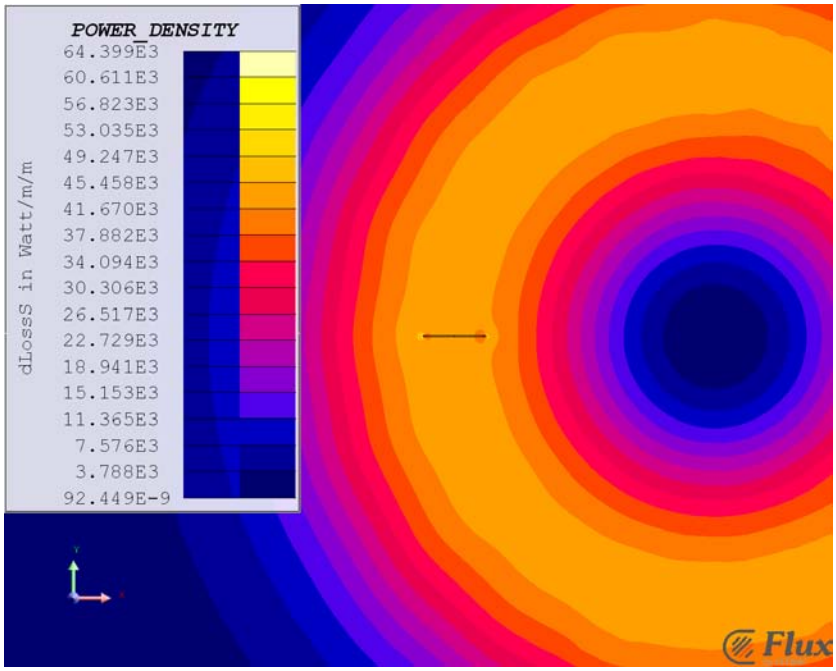

Figure 5.6: Power density distribution for Tra-X=12.5[mm]

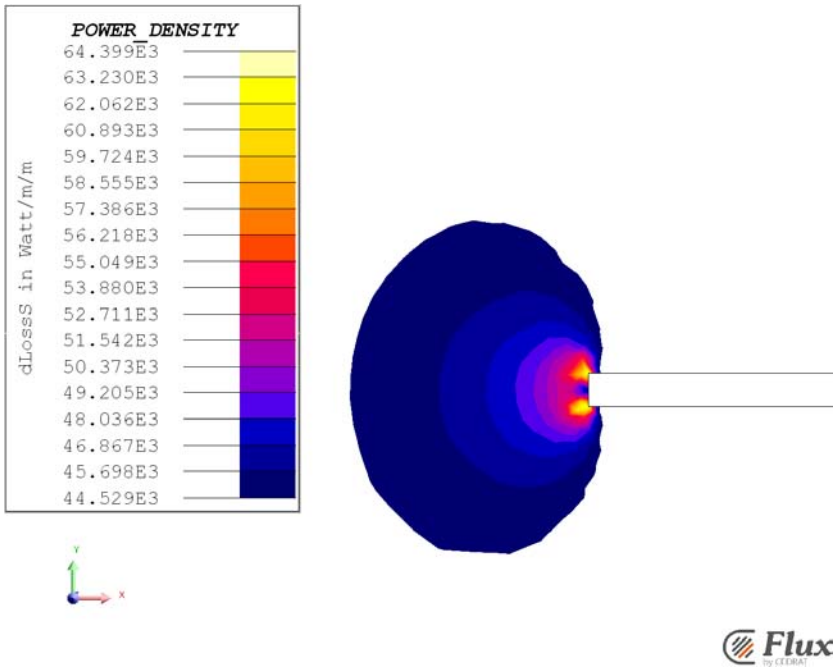

Figure 5.7: Power density distribution near the crack, Tra-X=12.5$[mm]$

5.4 Scenario: Translate Y

In this scenario, the coil conductor translates along y direction. In this case, the crack is perpendicular respects to the coil's translation's direction.

Parameter	Description	Value	Unit
I	current	100	$[A]$
f	frequency	400	$[kHz]$
$D-coil$	distance of the coil	2	$[mm]$
C	depth of the crack	0.03	$[mm]$
$Tra-Y$	translation along y	$0 \div 15$	$[mm]$

Table 5.4: Scenario *Translate Y* parameters

The same considerations of the previous scenario $Translate-X$ are valid for this case. The relative position of coil and defects changes the maximum value of current density and power density.

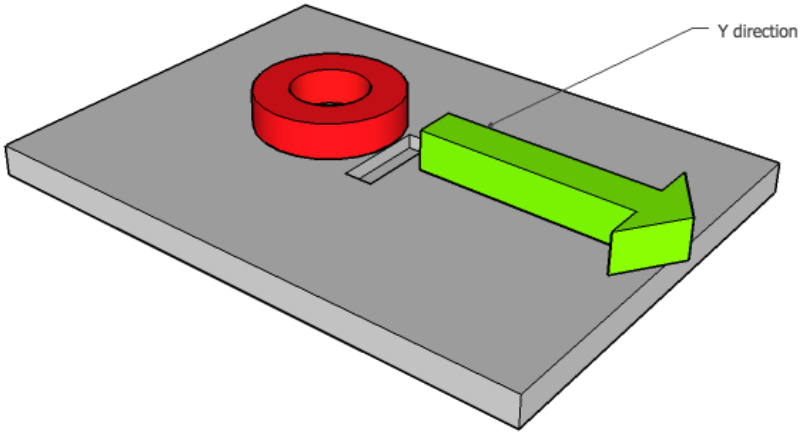

Figure 5.8: Graphic explanation of Scenario Translate-Y

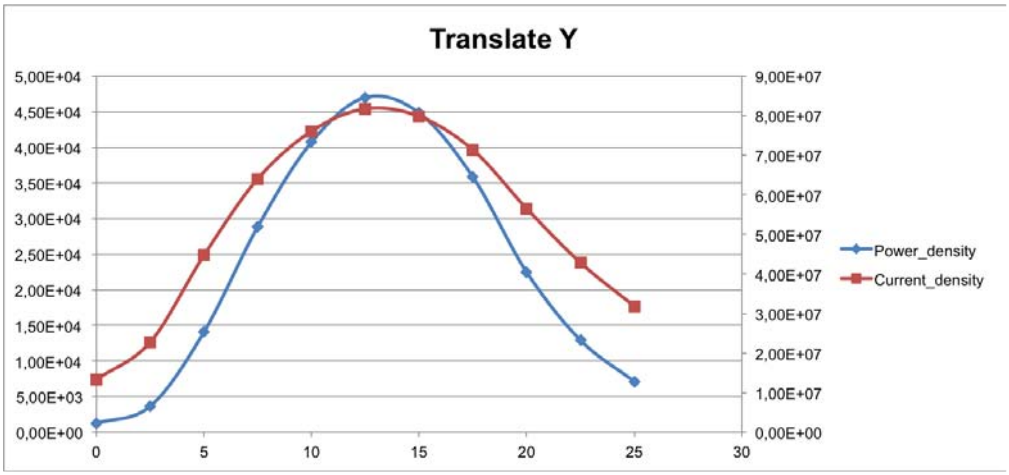

Figure 5.9: Variation of the current and power density in function of Tra-Y

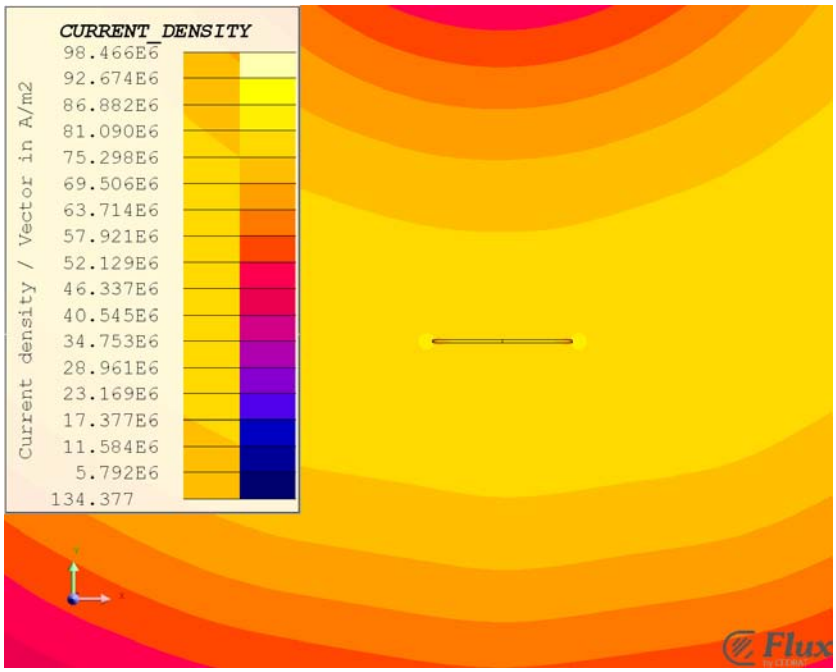

Figure 5.10: Current density distribution for Tra-Y=12.5[mm]

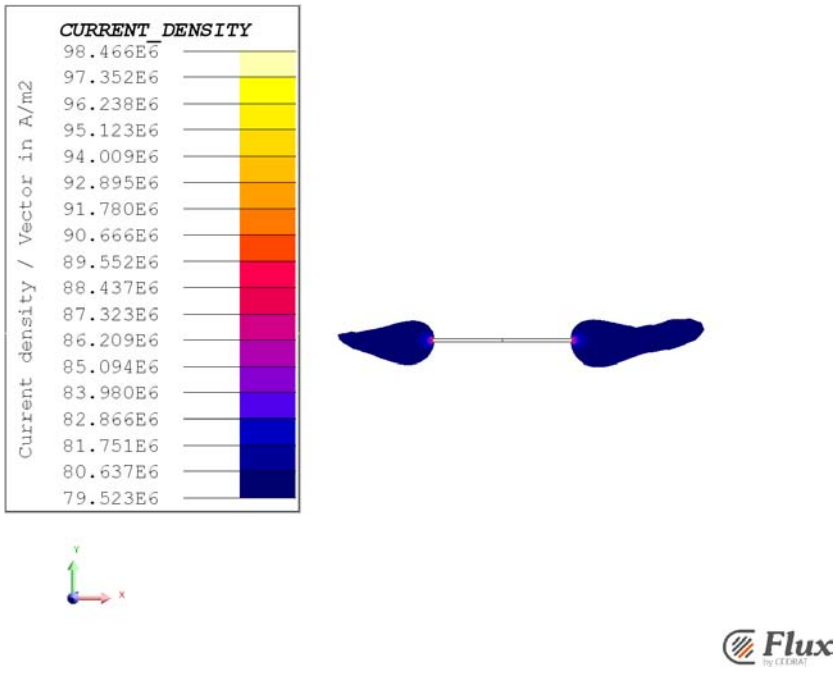

Figure 5.11: Current density distribution near the crack, Tra-Y=12.5[mm]

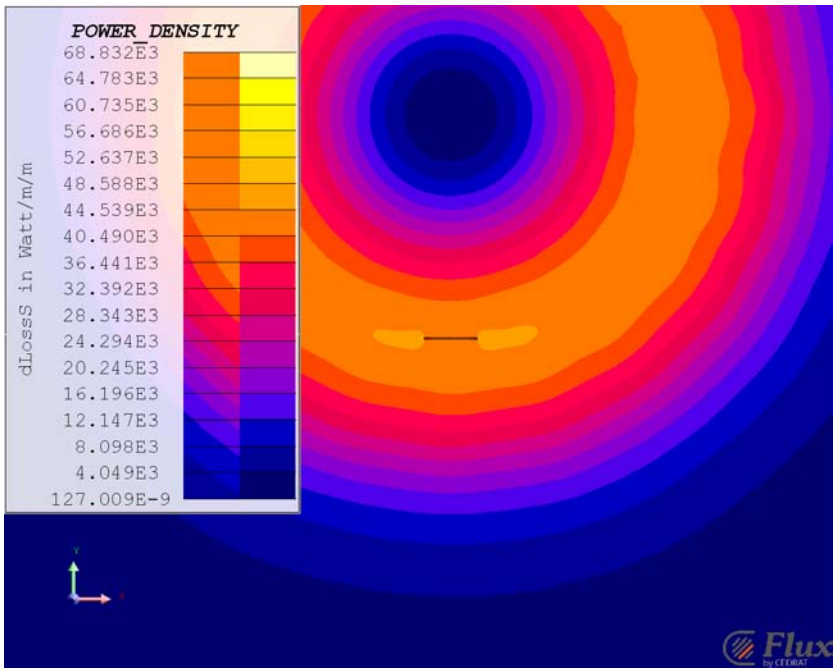

Figure 5.12: Power density distribution for Tra-Y=12.5[mm]

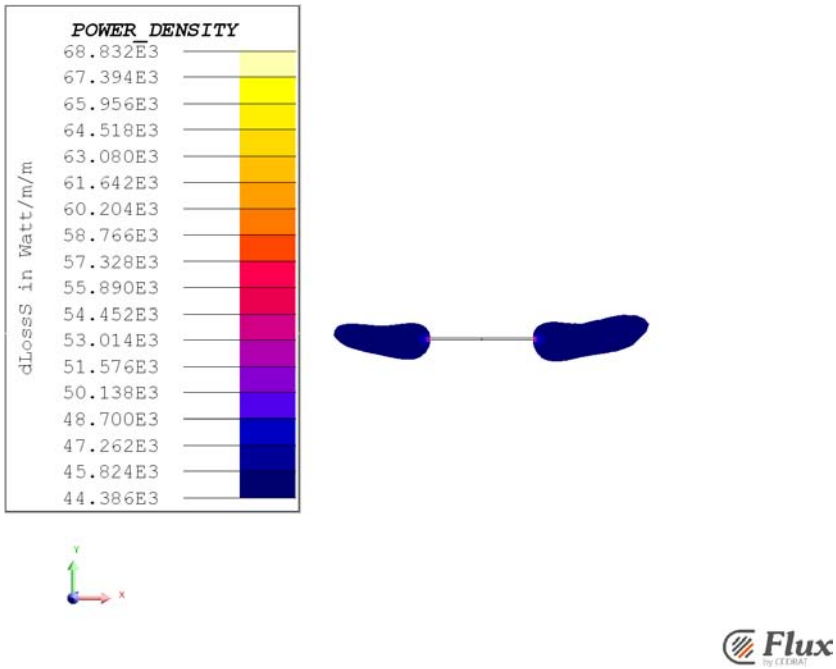

Figure 5.13: Power density distribution near the crack, Tra-Y=12.5[mm]

Chapter 6

Hairpin inductor

A cracked wide sheet of *Steel* is heated by an hairpin inductor. The coil translates along both directions x and y, scanning the load's surface. Two scenarios study the influence of the relative position between the coil and the defect. Due to the high frequency used the problem is studied with $T\omega$ surface impedance formulation.

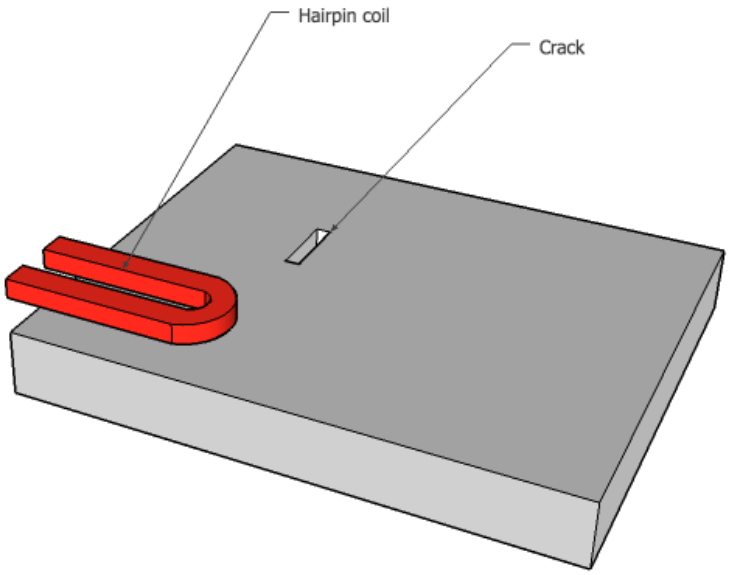

Figure 6.1: Schematic representation of the hairpin inductor and load

6.1 Geometry

The hairpin inductor is a *particular form of open-ended coil intended for pushing trough semi-closed or closed slots.* In this case hairpin inductor can be imagined as a U-shape coil conductor.
The geometry of the coil and the load, is parametrized as follow:

Parameter	Description	Formula	Value	Unit
Lx	width of the sample	-	200	$[mm]$
Ly	height of the sample	$2Lx$	400	$[mm]$
Lz	depth of the sample	–	1	$[mm]$
A	width of the crack	-	3	$[mm]$
B	height of the crack	-	0.06	$[mm]$
C	depth of the crack	-	0.03	$[mm]$
Dcoil	distance between load and coil	-	2	$[mm]$
Wcoil	width of the coil	-	5	$[mm]$
Hcoil	height of the coil	-	5	$[mm]$
Lcoil	length of the coil	-	30	$[mm]$
Ri	hole internal radius of the coil section	-	2.5	$[mm]$
Re	external radius of the coil section	-	7.5	$[mm]$

Table 6.1: Description of geometry of the hairpin inductor's case

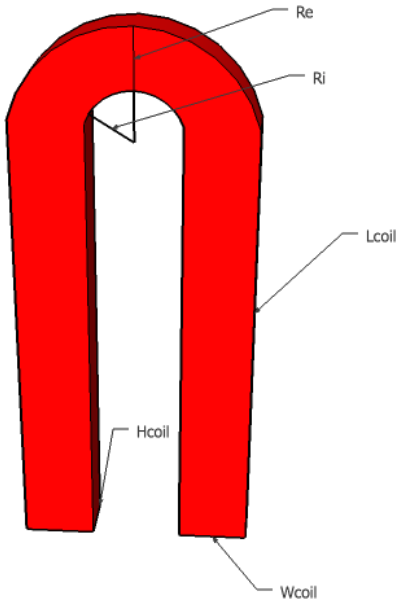

Figure 6.2: Schematic representation of the hairpin inductor

6.2 Scenario: Translate X

In this scenario, the hairpin inductor translates along x direction so the straight legs of the coil are perpendicular to the crack. Also in this case translation of the coil is possible because hairpin's center can be modified in function of the parameter $Tra - X$ and $Tra - Y$.

Parameter	Description	Value	Unit
I	current	100	$[A]$
f	frequency	400	$[kHz]$
$D - coil$	distance of the coil	2	$[mm]$
C	depth of the crack	0.03	$[mm]$
$Tra - X$	translation along x	$0 \div 15$	$[mm]$

Table 6.2: Scenario *Translate X* parameters

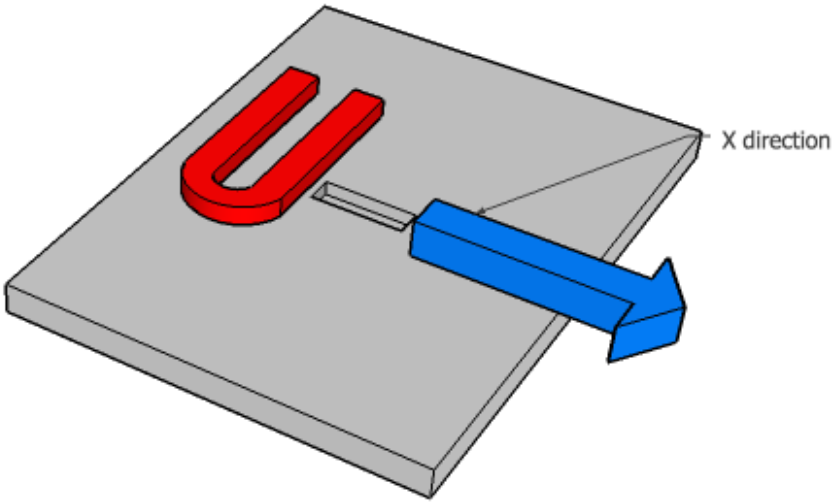

Figure 6.3: Graphic explanation of ScenarioTranslate-X

The simulation leads to the following considerations:

- the current and the power density evaluated and graphed for the point $(A/2; B/2, 0)$ reach the maximum value for $Tra - X \approx 7[mm]$, in correspondence of the highest value of eddy current induced in the load;
- the current density J is uneven distributed near the crack's edges, and

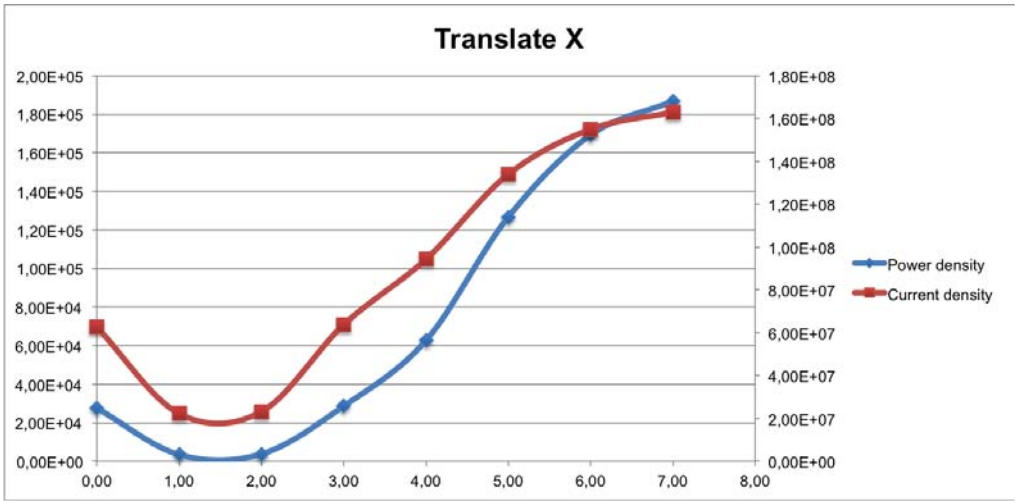

Figure 6.4: Variation of the current and power density in function of Tra-X

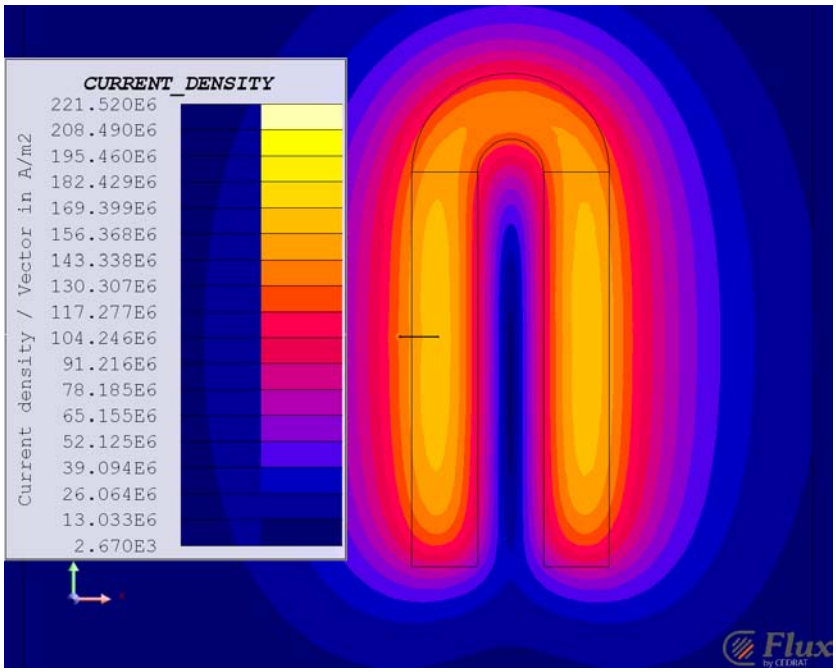

Figure 6.5: Current density distribution for Tra-X=7.5[mm]

the hot spot effect is more evident with hairpin inductor than with pancake coil. This is because the coil's geometry and relative position between inductor and load maximize the disturb effect of the defect.

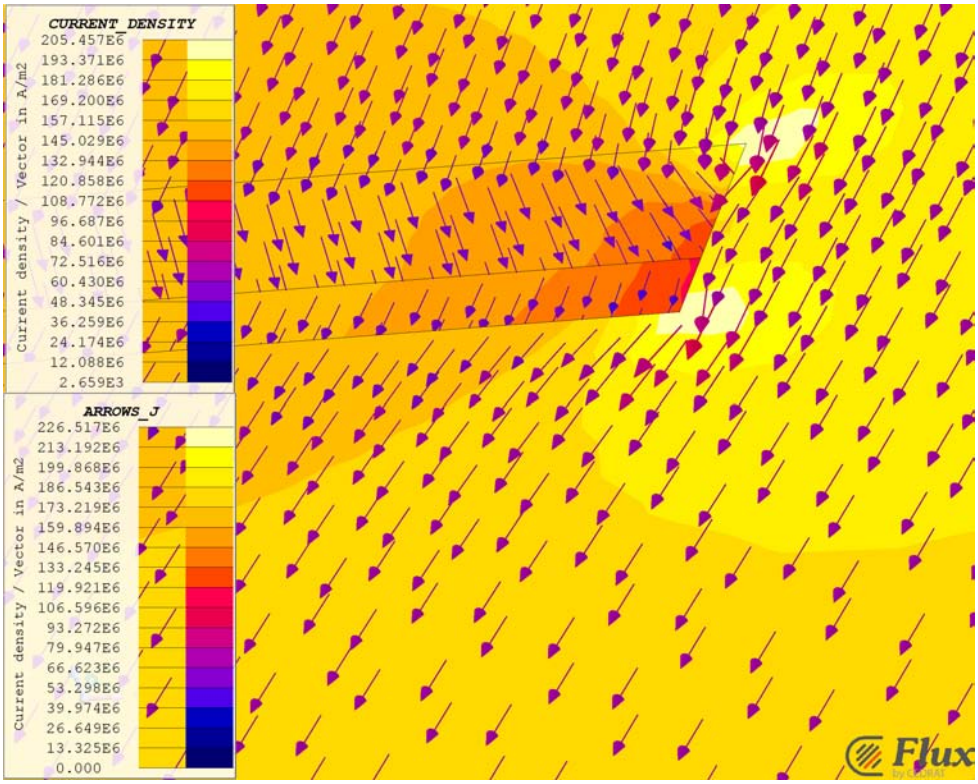

Figure 6.6: Current density distribution near the crack, Tra-X=7.5$[mm]$

6.3 Scenario: Translate Y

In this scenario, hairpin inductor has been rotated of 90°.
The hairpin inductor translates along y direction, in this way the crack is always parallel respect to the coil's legs.
An uneven distribution of current and power density can also be detected in this scenario, however as happened in the benchmark case, the hot spot effect is less remarked. This is due to the fact that crack is parallel respect to the current direction.

Parameter	Description	Value	Unit
I	current	100	$[A]$
f	frequency	400	$[kHz]$
$D-coil$	distance of the coil	2	$[mm]$
C	depth of the crack	0.03	$[mm]$
$Tra-Y$	translation along y	$0 \div 15$	$[mm]$

Table 6.3: Scenario *Translate Y* parameters

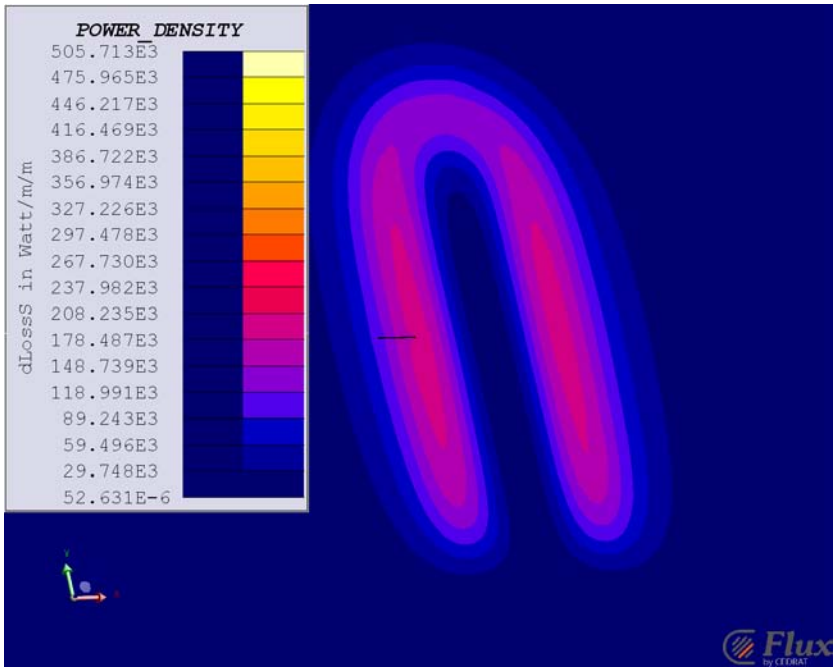

Figure 6.7: Power density distribution for Tra-X=7.5[mm]

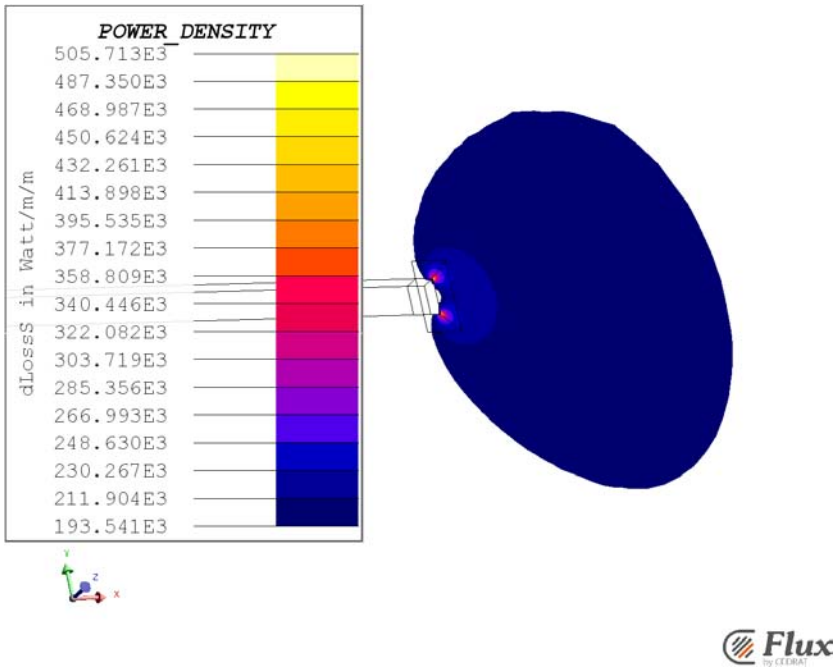

Figure 6.8: Power density distribution near the crack, Tra-X=7.5[mm]

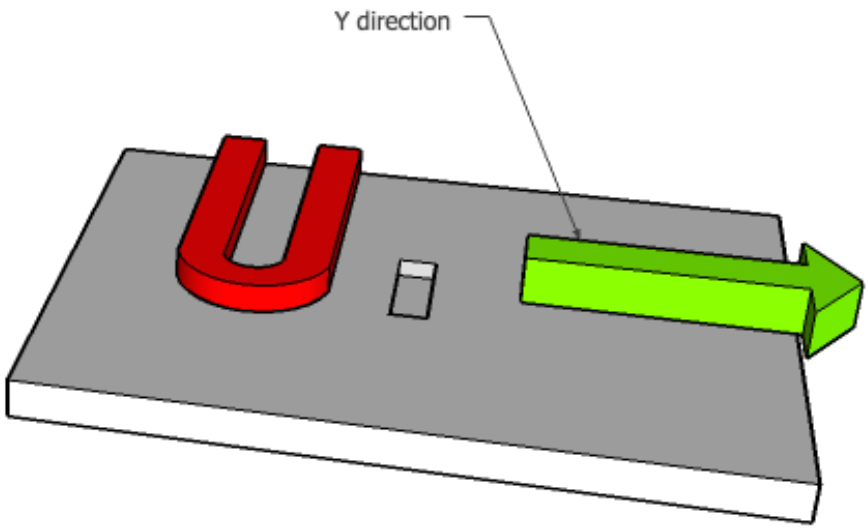

Figure 6.9: Graphic explanation of ScenarioTranslate-Y

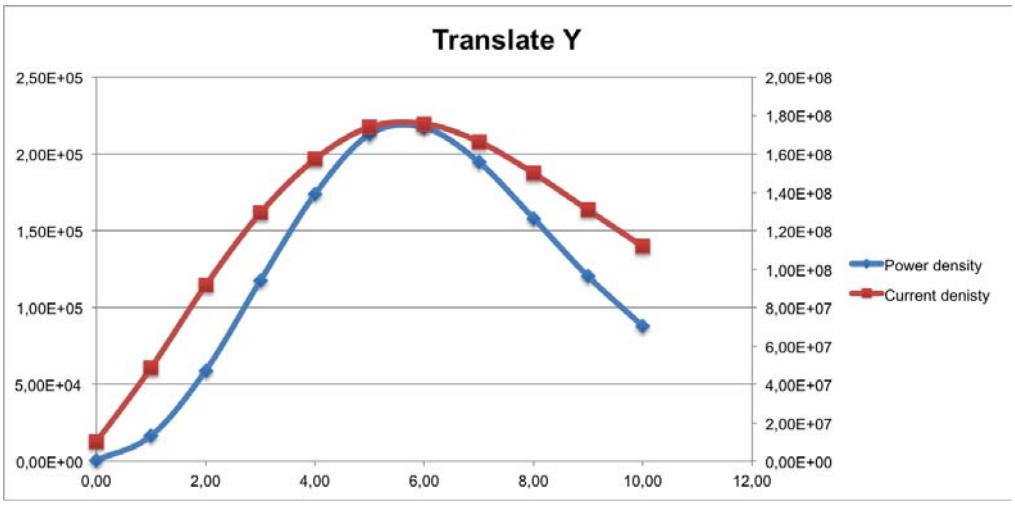

Figure 6.10: Variation of the current and power density in function of Tra-Y

6.4 Surface Impedance Thermal results

Surface Impedance simulations reaffirm the importance of using high frequency to boost the crack's disturb effect. With high frequency in fact, the

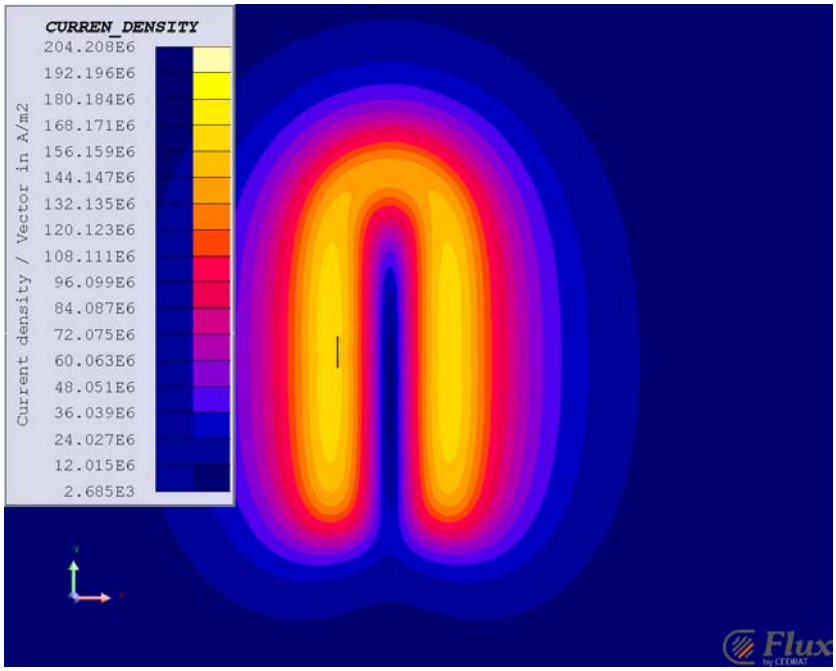

Figure 6.11: Current density distribution for Tra-Y=7.5[mm]

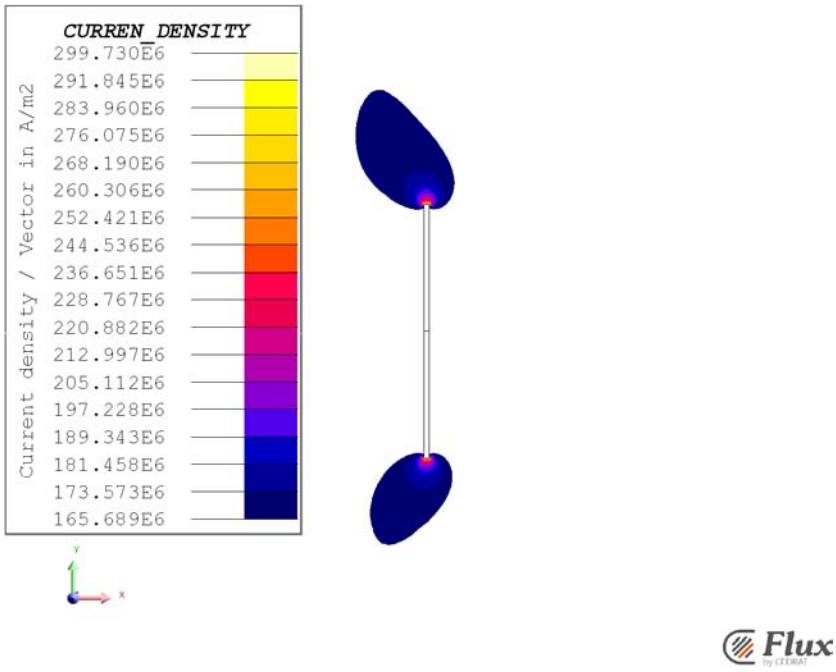

Figure 6.12: Current density distribution for Tra-Y=7.5[mm]

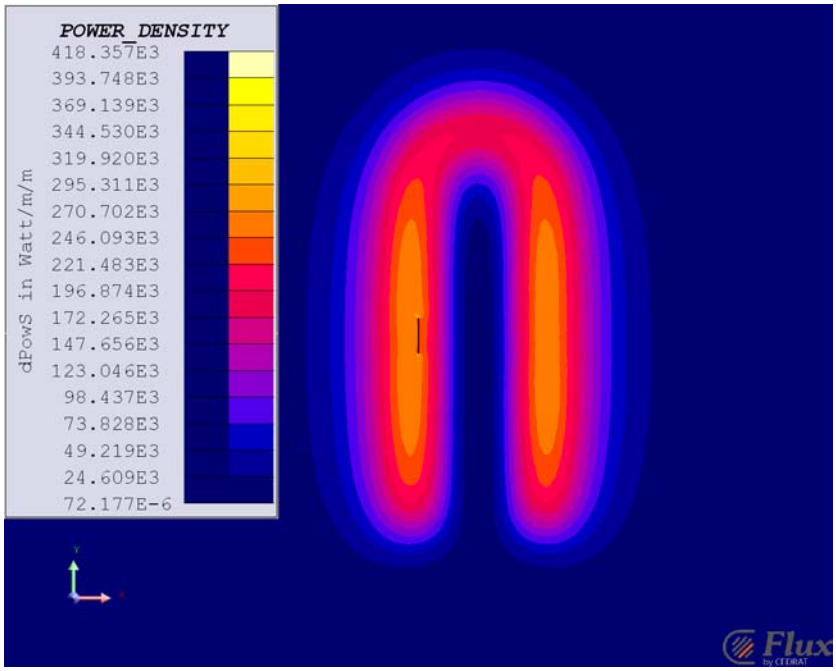

Figure 6.13: Power density distribution for Tra-Y=7.5[mm]

current and power density is higher in the neighborhoods of the crack.
Unfortunately temperature distribution can not be evaluated directly from the simulations.
Temperature is however evaluated with an approximated method based on the evaluation of the total power dissipated near the crack.
The power is evaluated as surface integral for the $In-Area$ and $Out-Area$.
The results are then transferred in a thermal model, where they become the power sources for the thermal solution. Clearly the method used is less precise than a straight forward magneto-thermal analysis, therefore the results are deeply conditioned by the method.

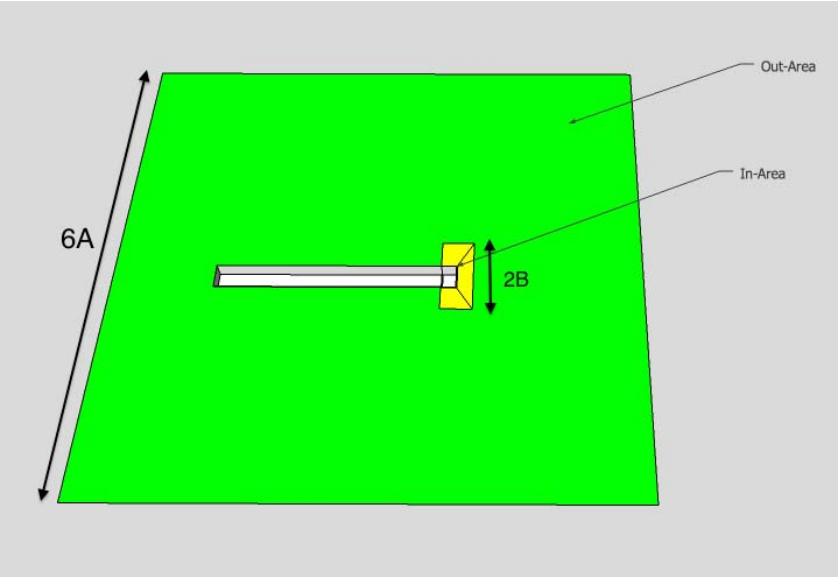

Figure 6.14: In and Out Area used for temperature distribution evaluation

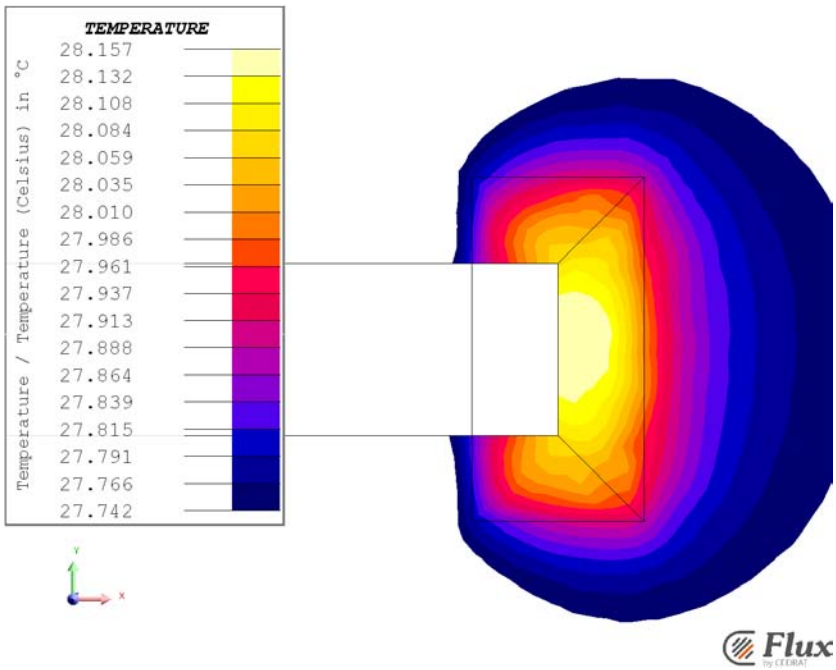

Figure 6.15: Temperature distribution near the crack

Chapter 7

Conclusions

Both the Benchmark and the Surface Impedance simulations reveal an uneven distribution of current and power densities near the crack edges. In particular, there seems to be a relation between the depth of the crack and the frequency used for the test. The method allows the evaluation of the width of the defects, that can be computed as the distance between the two hotspots generated near the crack edges.
In the Benchmarck simulation, an appreciable rising of the temperature near the defect is observed.
Simulations resulting from AV formulation on nodal finite elements are affected by discretization errors and unrealistic current density distribution near the crack edges. This result is according to Biró [11]. The solution for induced power density can not be considered reliable mostly for high frequencies even if the mesh is refined. Thus, a second model has been developed for both pancake and hairpin simulations, where the steel surface is modeled by surface impedance condition. This formulation allows for reliable results at high frequencies. An approximated thermal model has been coupled to the electromagnetic model for the evaluation of the temperature distribution.
In order to define an automatic procedure for the detection of surface cracks, the influence of crack orientation in respect to coil position has been investigated. Pancake coil seems the best choice for an automatic detection of the defects. Hairpin inductor as well as linear inductor are affected by the relative position between inductor and crack.
Further numerical analysis and laboratory test are needed in order to test thermographic detection method on ferromagnetic materials and other types of defects in order to understand the advantages and drawbacks of this method.

Bibliography

[1] Forzan M.,"Metodologie di simulazione con il metodo FEM di problemi relativi a test non distruttivi con correnti indotte", PhD thesis, Universitá Degli Studi Di Padova, 2000;

[2] Lupi S.,"Appunti di elettrotermia", A.A. 2005-2006;

[3] Spezzapria M., "Simulazione numerica del processo di tempra ad induzione di ruote dentate per l'industria aeronautica", Master thesis, Universitá Degli Studi di Padova, 2011;

[4] Ciccarone L.,"Models and test of induction contour hardening process", Master thesis, Universitá Degli Studi Di Padova, 2014;

[5] Ilham M. Z. A.,"Modeling and experimental investigation of eddy current distribution for angular defect characterization", PhD thesis, School of Electrical, Electronic and Computer Engineering Newcastle University, 2010;

[6] Tsopelas N. , Siakavellas N.J.,"Electromagnetic-thermal NDT in thin conducting plates", Department of Mechanical Engineering and Aeronautics, University of Patras, 2006;

[7] Willcox M., Downes G.,"A brief description of NDT techniques", Insinght NDT Equipment Ldt, The Old Cider Mill Kings Thorn Herefordshire, 2000;

[8] Minella M.,"Algoritmi di elaborazione di immagini termiche per analisi dei difetti superficiali: su componenti in fibre composite di carbonio e in acciaio", Master thesis, Universitá Degli Studi Di Padova, 2013;

[9] Jelicic B., "Steel billet through heating: experimental validation of numerical model EM-TH coupled ", Master thesis, Universitá Degli Studi di Padova, 2013;

[10] Dalla Rizza N., "Prove non distruttive con correnti parassite e magnetoscopia: applicazioni e analisi dei risultati", Master thesis, Universitá Degli Studi di Padova, 2009;

[11] Biró O., "Edge element formulations of eddy current problems", IGTE, Technical University of Graz, Kopernikusgasse, 1997;

[12] Alotto P., "Appunti di elettrotecnica computazionale",Universitá Degli Studi Di Padova, 2013-2014;

[13] Kelliher D., "Notes from the course of finite element analysis", University College of Cork, 2013.